An interactive cellular ecosystem blocks epithelial transformation in naked mole-rat

Mikaela Behm[1,#], Pablo Baeza Centurión[2,#], Luca Penso-Dolfin[2], Francisco Javier Botey Bataller[2], Nick Hirschmüller[2], Sylvain Delaunay[1], Marie-Luise Koch[3], Stefania Del Prete[3], Daniela Sohn[1], Celine Reifenberg[1], Meike Schopp[3], Fritjof Lammers[3], Llorenç Solé-Boldo[4], Jeleana Dutton[5], Sabine Begall[6], Walid T. Khaled[7], Ewan St. J. Smith[7], Duncan T. Odom[3,5]*, Michaela Frye[1]*, and Angela Goncalves[2]*

[1] German Cancer Research Center (DKFZ) - Division of Mechanisms Regulating Gene Expression, 69120 Heidelberg, Germany; [2] German Cancer Research Center (DKFZ) - Somatic Evolution and Early Detection, 69120 Heidelberg, Germany; [3] German Cancer Research Center (DKFZ) - Division of Regulatory Genomics and Cancer Evolution, 69120 Heidelberg, Germany; [4] German Cancer Research Center (DKFZ) - Division of Epigenetics, 69120 Heidelberg, Germany; University Hospital Heidelberg, 69120 Heidelberg, Germany; [5] Cancer Research UK Cambridge Institute, University of Cambridge, Li Ka Shing Centre, Cambridge, CB2 0RE, UK; [6] Department of General Zoology, Faculty of Biology, University of Duisburg-Essen, 45147 Essen, Germany; [7] Department of Pharmacology, University of Cambridge, Cambridge CB2 1PD, UK

# Equal contribution
* Co-corresponding

Abstract

The mechanisms underlying cancer resistance in long-lived organisms are largely unexplored. Here, we report how naked mole-rats (*Heterocephalus glaber*) resist tumorigenesis when exposed to potent skin carcinogens. Single-cell transcriptional analysis of homeostatic full-thickness naked mole-rat skin revealed higher epidermal turn-over, a distinct composition of dermal extracellular matrix (ECM) and fewer resident T-cells, when compared to mouse and human. Carcinogenic treatment of skin generated the expected mutational landscape, but unlike in the mouse, failed to stimulate T-cells or generate tumours. Instead, naked mole-rat accelerated epidermal turnover to shed mutant cells. At the same time, the ECM was extensively remodelled via enhanced anti-inflammatory communication among fibroblasts and between fibroblasts and epidermal cells, creating a tumour-suppressive microenvironment. We demonstrate that, in contrast to mouse, naked mole-rat dermal fibroblasts lack intrinsic tumour-promoting capabilities *in vitro* and *in vivo*. Our results demonstrate that the cellular ecosystem of naked mole-rat skin actively suppresses epithelial transformation.

Introduction

Naked mole-rats (*Heterocephalus glaber*) are mouse-sized, eusocial, subterranean rodents with exceptional longevity (>30 years) [1] and high natural cancer resistance [2]. Although their cells can transform in the presence of oncogenes [3,4], less than ten neoplasms have ever been observed in thousands of captive animals [1,5-8]. Naked mole-rat organs resist cancer formation when challenged with carcinogens *in vivo* [9], yet how naked mole-rats circumvent malignant transformation is not fully understood. Both cell autonomous and non-autonomous mechanisms have been suggested, including high expression of DNA repair signalling genes [10,11], heightened sensitivity to contact-inhibition, communication with the extracellular environment [12-15], slow somatic mutation rates [16], and a deficient necroptosis response that dampens immune cell infiltration [9].

Most cancers arise in epithelial tissues, and squamous cell carcinoma (SCC) is one of two most frequent skin cancers [17,18]. The most commonly used preclinical animal model of SCC is carcinogen-exposed mouse skin [19]. In the classical two-stage chemical skin carcinogenesis model, initiation is achieved by induction of DNA mutations using a single dose of 7,12-dimethylbenz[a]-anthracene (DMBA), a polycyclic aromatic hydrocarbon, followed by stimulated epidermal proliferation via repeated treatment with tetradecanoyl-phorbol acetate (TPA) [20]. In this protocol, carcinogenesis in mice is driven by the same spectrum of genomic alterations found in humans [21]. For example, DMBA commonly induces an activating mutation in mouse *Hras* [22-24], a driver frequently found in human cutaneous SCC [25] and combined with *SV40LT* and $HRAS^{G12V}$ is oncogenic in naked mole-rats [4]. The value of mouse models for human cancer is however limited as humans are comparatively more long-lived and resistant to cancer [26].

Here, we combine single-cell transcriptional analysis of 395,217 naked mole-rat, mouse, and human skin cells with two-stage skin carcinogenesis experiments to comprehensively resolve the cellular compositions and interactions during homeostasis and upon cancer induction. This systematic comparison reveals the unique combination of novel intrinsic molecular and cellular mechanisms exploited by this archetype long-lived mammal to achieve cancer resistance.

Results

Naked mole-rat skin is maintained in a distinct immune suppressive environment

Naked mole-rat skin is histologically similar to human skin, a stratified squamous epithelium with very few hair follicles (Fig. 1a-d and Extended Data Fig. 1a-d) [27]. As expected, we found that undifferentiated basal layer cells express keratin 14 (KTR14), while differentiated suprabasal cells labelled positive for KRT10 (Extended Data Fig. 1b-c). Unexpectedly, our immunofluorescence labelling revealed high levels of co-expressed KRT6 in naked mole-rat suprabasal cells (Extended Data Fig. 1d), which is commonly associated with altered proliferation, cell adhesion, and migration in response to wounding [28].

To quantify the cell types found in each species, we generated single cell transcriptomes of full thickness skin biopsies from six naked mole-rats (n = 21) and three mice (n = 9), and compared them to five humans (n = 5) [29]. Using established marker genes, we identified separately in each species: T-cells, antigen presenting cells (APCs), endothelial cells, fibroblasts, epithelial cells, mast cells, muscle cells, Schwann cells and melanocytes (Fig. 1e-h and Extended Data Fig. 1e) [29-32].

To cross-map cell types between species, we used three complementary strategies. First, we used 12,940 unambiguously orthologous genes to integrate the three species' transcriptomes

using reciprocal principal component analysis (*Methods*) followed by unsupervised clustering (Extended Data Fig. 1h-i) [33] and then, manually annotated cell types using marker genes. Second, we used an automated cell-type classifier based on marker genes (*Methods*). Third, for the small fraction of cells for which the single-species and the integrated 3 species cell type annotation disagreed (Extended Data Fig. 1i), we trained a deep learning classifier to find a consensus annotation (*Methods*). These analyses revealed a surprising degree of species-specificity in the cell type composition of skin, consisting of five transcriptionally distinct clusters capturing epithelial, fibroblasts, APC, T-cell, and endothelial compartments (Fig. 1e-l).

Our fully integrated analysis revealed three unique features of homeostatic naked mole-rat skin. First, when compared to human (9.9% ± 4.4) and mouse (6% ± 2.5), naked mole-rat skin has very few T-cells (2.1% ± 0.7) (Fig. 1e-l and Extended Data Fig. 1f-h). In other tissues, such as spleen and blood, naked mole-rats have a similar proportion of T-cells as mouse (~30%) (Extended Data Fig. 1f-g) [34]. Second, naked mole-rat cell types are transcriptionally divergent from mouse and human, and their compositional proportion in skin also differs (Fig. 1e-m; Extended Data Fig. 1j). Third, naked mole-rats showed an attenuated potential for activating inflammatory responses, and modulation of cell adhesion molecules in all cell types (Fig. 1n).

Our data suggested the naked mole-rat's suppressed inflammatory landscape during homeostasis may be shaped by a globally altered expression of adhesion proteins. Cell adhesion molecules play a vital role in immune cell trafficking into tissues, effector cell activation and proliferation during homeostasis, inflammation and cancer [35]. For instance, fibroblasts had altered expression of cell adhesion proteins (F2, PCDHGC5, NRXN1, SULF1, TMEM176A, TMEM176B, DPEP1, GLDN) (Fig. 1m) and dysregulated production of cytokine interleukin-

140 8 (IL-8), a key pro-inflammatory mediator of leukocyte recruitment via altered focal adhesions (Fig. 1n) [36].

In sum, naked mole-rat skin has a distinct and immune suppressive environment, likely shaped by the species-specific network of cell adhesion molecules.

145

Naked mole-rats resist an extreme cancer induction protocol

We tested whether species-specific tissue composition contributes to tumour resistance in naked mole-rats [9] by subjecting mouse and naked mole-rat to powerful carcinogens, followed by single-cell sequencing of full thickness skin biopsies (including two papillomas in mouse) 150 (*Methods*). In mouse, skin cancer is initiated by a single application of DMBA followed by repeated treatment with TPA to drive proliferation (Extended Data Fig. 2a) [20]. Under this standardized protocol, all mice developed papillomas, benign epithelial tumours, around 10 weeks (Fig. 2a and Extended Data Fig. 2b) [20]; but naked mole-rats resisted the standard DMBA/TPA treatment for up to two years [9]. Therefore, we adapted a more intensive protocol 155 developed to produce skin lesions in similarly cancer-resistant blind mole-rats (*Spalax ehrenbergi*) by increasing concentrations of both DMBA and TPA by 5-fold and inducing the application frequency of TPA to three times per week [37].

To our surprise, no treated naked mole-rat developed tumours or any macroscopic skin 160 alteration following six months of this rigorous treatment (Fig. 2a and Extended Data Fig. 2b).

We considered the possibility that naked mole-rat cells may have evolved mechanisms to neutralize the mutagenicity of DMBA, thus preventing somatic mutations. To test this, we deeply sequenced the exomes of DMBA-treated mouse and naked mole-rat full-thickness skin

165 biopsies (*Methods*). DMBA treatment produces mainly T-to-A (T>A) transversions in a specific sequence context [21,38], and this signature was readily identified at the variant allele frequency (VAF) expected for clonal expansions in all treated mouse and naked mole-rats (Fig. 2b-d). Notably, only naked mole-rats exhibited excess C>A transversions, which in mouse are considered late mutations often occurring subclonally in metastases [38]. Thus, similar to mouse,
170 naked mole-rat skin is highly susceptible to DMBA mutagenesis, and acquires somatic mutations.

We also considered the possibility that naked mole-rat cells can resist the proliferation in skin caused by TPA treatment, which triggers cell cycling via protein kinase C family [39,40]. This
175 was not the case: as in mouse, treatment of naked mole-rat skin with TPA for 12 weeks resulted in epidermal thickening (Fig. 2e-f and Extended Data Fig. 2c-d) and enhanced proliferation (Fig. 2g-h).

In sum, naked mole-rat skin resists tumour formation, even when challenged by an
180 exceptionally strong carcinogenic treatment regime that successfully induced somatic mutations and enhanced proliferation.

Immune response to carcinogenesis is blocked in naked mole-rat

We therefore considered the possibility that inherent differences in how naked mole-rat skin's
185 ecosystem responds to DMBA/TPA treatment could inhibit tumour formation. We first compared the cell type composition of full thickness mouse and naked mole-rat skin before and after DMBA/TPA treatment using single-cell transcriptional profiling (Extended Data Fig. 2e-f). Strikingly, T-cell numbers remained constant in naked mole-rat skin, whereas mouse skin showed a 3-fold increase (Fig. 2i), as expected [41]. We independently confirmed the low

190 number of T-cells in DMBA/TPA-induced naked mole-rat skin by labelling for CD3 (Fig. 2j-l), present on 95% of T-cells in both epidermis and dermis [42-44]. The number APCs was largely unaffected (Extended Data Fig. 2g).

We then asked whether the T-cell population remained stable in naked mole-rats because it
195 was inert to the DMBA/TPA treatment. However, T-cells exhibited a strength of transcriptional response to the treatment, comparable to all other major skin cell types (Fig. 2m and Extended Data Fig. 2h). Similar to homeostatic skin (Fig. 1), we found that the transcriptional responses in naked mole-rat caused by DMBA/TPA in all cell types were diverged from mouse. We used a machine-learning classifier [45] to identify that naked mole-rat T- and fibroblasts had the
200 greatest transcriptional perturbations upon DMBA/TPA treatment; in contrast, epithelial cells directly exposed to the chemicals and eventually forming the tumour have the lowest (*Methods*, Fig. 2n). Thus, our data indicated that epithelial transformation resistance in response to DMBA/TPA was mostly modulated by the immediate environment of the epithelial cells.

205 We therefore compared what functional gene set in each cell type were up- and down-regulated by treatment with DMBA/TPA using gene set enrichment analysis (*Methods*) [46,47]. We found that APCs up-regulated DNA repair in both species (Extended Data Fig. 2i-j). Mouse T-cells upregulated cytokine signalling, including BHLHE40 that activates leukocytes and induces T-helper 17 (Th17) cell polarization (Fig. 2m, o and Extended Data Fig. 2k; lower panel) [48,49].
210 Such Th17 polarization is tightly linked to cancer [50]. In stark contrast, naked mole-rat T-cells actively suppressed the same cytokine signalling pathways (Fig. 2p), and instead activated a wound healing response (Extended Data Fig. 2l; upper panel). The lack of immune responses in naked mole-rats was likely due to fibroblasts repressing cytokine signalling pathways in response to the carcinogenic insult (Fig. 2q and Extended Data Fig. 2l).

The dermal compartment provides structural support of the skin by producing the ECM, a complex network of proteins and proteoglycans secreted by epidermal cells, fibroblasts and immune cells. Although DMBA/TPA treatment induced ECM remodelling in both naked mole-rat and mouse fibroblasts (Extended Data Fig. 2m), this remodelling had different functional implications for the two species. Mouse fibroblasts synthesized COL12A1, a component of a pro-cancerous microenvironment [51]; naked mole-rat fibroblasts upregulated ECM components required for maintaining skin homeostasis and creating an immunosuppressive stromal niche, such as ECM1 and GAS6 [52,53].

Finally, our analysis of epithelial cells in naked mole-rats revealed enhanced wound healing responses (Fig. 2r), indicating altered balance between proliferation and differentiation towards accelerated epithelial turnover. Fast turnover requires a coupled acceleration of stem cell division and differentiated cell death, suggesting a tumour suppressive strategy by which increased cell differentiation can wash out mutants [54].

High cellular turn-over and early differentiation maintain the naked mole-rat epidermis

Testing this hypothesis required us to first create high resolution maps of the actively differentiating interfollicular epidermis (IFE) at homeostasis. We integrated and clustered epithelial cells from the three species using the uniquely mapping orthologous genes, and identified cell types using known marker genes (Fig. 3a, Extended Data Fig. 3a). Mouse had substantial contributions from sebaceous glands and hair follicles, as expected (Fig. 3a-b; coloured cells); these cell types were removed from further analyses. We then ordered the remaining interfollicular epidermal cells by differentiation status (Fig. 3c).

240 This revealed a continuous differentiation trajectory that began at undifferentiated cells with high KRT14 expression, and continued through cell states with gradually increasing expression of commitment and terminal differentiation genes (Fig. 3c and Extended Data Fig. 3a). In homeostatic skin, we observed multiple short branching events that captured cells in a hybrid state, simultaneously expressing undifferentiation (KRT14) and early differentiation (KRT10)
245 marker genes (Hybrid I) (Fig. 3c, light orange cells; Fig. 3d, $K14^{hi}/K10^{hi}$). We identified a second hybrid state (Hybrid II) further along the differentiation trajectory (Fig. 3 c-d). In homeostasis, both hybrid states were significantly enriched in naked mole-rat epidermis (Fig. 3e-f).

250 We confirmed in healthy naked mole-rat skin that the undifferentiation (KRT14 or KRT5) and commitment (KRT10) markers were co-expressed within the same cell on RNA and protein levels in both the basal and suprabasal layers (Fig. 3g and Extended Data Fig. 3c-d). Such a hybrid population simultaneously expressing progenitor- and differentiation-related keratins was previously reported in newborn mice and neonatal human foreskin [55,56]. We confirmed that
255 the developing mouse epidermis contained KRT14/KRT10 co-expressing cells postnatally (P1 to P9) when proliferation rates are the highest [57], yet their localisation in the basal layer in both mouse and human was extremely rare (Extended Data Fig. 3e-i). Regardless, this newly discovered hybrid population represents proliferating cells committed to differentiation [58-60].

260 Thus, the increased presence of hybrid cells in homeostasis supports a model wherein the naked mole-rat balances a naturally high turn-over of epidermal cells by accelerating differentiation.

Enhanced turn-over protects naked mole-rat epidermis against carcinogenic insults

We reasoned that the accelerated turn-over and differentiation in naked mole-rat skin might alter how the epidermis responds to carcinogens, when compared to mouse. To do so, we tested for differential abundance of the different cell types upon treatment (*Methods*). Despite a thickening of the epidermis upon DMBA/TPA treatment (Fig. 2e-f), the overall proportions of individual epithelial cell states were unaffected in naked mole-rats, confirming a balanced turnover (Fig. 3h and Extended Data Fig. 3b). In contrast, the mouse epidermal composition changed following DMBA/TPA, by triggering cell cycle and imbalancing cell proportions in both undifferentiated and differentiated lineages (significant changes in cell type proportions in mouse are shown with arrows in Fig. 3h).

Interestingly, the fraction of cycling cells in naked mole-rat epidermis during homeostasis was appreciably greater than in mouse (Fig. 2h, 3h). Therefore, we compared the proliferative capacity of naked mole-rat and mouse IFE by performing immunofluorescent labelling for marker of proliferation Ki-67 (MKI67) (Fig. 3i). During homeostasis, naked mole-rat epidermis contained a larger population of cycling progenitor cells in the basal layer (Fig. 3i-j, left panels; arrowheads). In line with the finding that hybrid cells can cycle, the naked mole-rat suprabasal layer, which in mouse consists overwhelmingly of terminally committed epithelial cells, additionally contained 17% of all MKI67-positive cells (Fig. 3i-j; asterisks). Following DMBA/TPA-treatment, the MKI67-positive suprabasal population in naked mole-rat further expanded and co-expressed KRT14, suggesting that these cells may be the Hybrid I/II cells (Fig. 3c-i). In mouse, a similar population is only found in treated, hyperplasic skin (Fig. 3i-j).

The population of committed KRT10-positive cells in the undifferentiated basal layer, decreased upon carcinogen treatment in naked mole-rats (Fig. 3k-l), indicating expansion of

uncommitted progenitor cells. In contrast, mouse epidermis showed the opposite trend (Fig. 3l). To independently estimate the progenitor replacement rates in mouse and naked mole-rat epidermis, we called mutations on the DMBA-treated skin and calculated their variant allele frequencies. These were used to estimate clone sizes and subsequently fit a model of stem cell division (*Methods*) (Fig. 3m) [61]. Naked mole-rat epidermis had a progenitor replacement rate that was approximately two times higher than in mice (Fig. 3n).

Thus, naked mole-rats have evolved robust and balanced mechanisms to shed mutated epithelial cells by counterbalancing increased proliferation with accelerated differentiation.

DMBA/TPA induces remodelling of the upper dermis in naked mole-rats

In adult organs, epithelial differentiation is supported by the underlying stroma [62]. The dermal stroma consists of distinct fibroblast populations that can promote skin cancer development by maintaining chronic inflammation [63]. Therefore, we next determined how DMBA/TPA treatment alters the stroma by clustering fibroblasts from naked mole-rat, human and mouse skin (Fig. 4a). The continuous nature of these fibroblast clusters, in which adjacent clusters overlap, suggests gradually shifting cellular identities among different subtypes (Fig. 4a). Nevertheless, we discovered two distinct fibroblast subtypes (Fibroblast II and VI) only shared between human and naked mole-rat (Fig. 4b and Extended Data Fig. 4a). The fraction of fibroblast subtypes shared among the three species was variable (Fibroblast I, III, IV, V) (Fig. 4b, rows 1-6). Mouse fibroblasts were frequently found in species-specific states not shared with naked mole-rats or humans (Fig. 4b, rows 7-15); those states might be related to hair follicle cells [64,65]. As expected, also the emergence of cancer associated fibroblasts (CAFs) was unique to mouse (Fig. 4b, row 15) [63,66].

The dermis can be divided into two morphologically distinct layers: the upper papillary dermis immediately beneath the epidermis and the deeper reticular dermis. In mouse and human, the transcriptomes of fibroblasts can reflect their spatial depth within the dermis.[29,31,67] Using these transcriptional signatures containing validated genes, we scored each class of naked mole-rat fibroblast for its dermal depth (Fig. 4c and Extended Data Fig. 4d). This analysis identified Fibroblasts I-III as in the lower dermis and Fibroblasts IV-VI as located in the upper dermis (Fig. 4c and Extended Data Fig. 4b).

Treatment with DMBA/TPA appeared to cause the population of fibroblasts in the lower dermis (Fibroblast II and III) to increase at the expense of fibroblasts in the upper dermis (Fibroblast IV-VI) (Fig. 4b). Furthermore, the post-treatment transcriptomes of the remaining upper dermal fibroblasts (Fibroblast IV-VI) suggest these were shifted in depth as well (Fig. 4c). This was supported by a corresponding increase in the gene expression signature specifically associated with fibroblast migration (Fig. 4d-e) and, in naked mole-rat, we confirmed a reduced cellularity in the upper dermis (Fig. 4f-g and Extended Data Fig. 4e). Fibroblasts migrating to the deeper dermis in naked mole-rat might be a direct consequence of tissue damage caused by DMBA/TPA.

Naked mole-rat fibroblasts do not create a pro-inflammatory tumour environment

We therefore tested whether the inter-fibroblast communications change following DMBA/TPA challenge in naked mole-rat skin (*Methods*) (Fig. 4h-i) [68]. After treatment, communication between all fibroblast subtypes was increased, reflecting the appearance of novel ligand-receptor interactions (Fig. 4i). These novel cell-cell interactions were associated with extensive remodelling of ECM components (*Methods*) (Fig. 4j). A core function of fibroblasts is to regulate the production of collagen, which generates mechanical forces that

control physiological processes and its dysregulation can contribute to cancer [69]. Across all naked mole-rat fibroblasts, we identified an average of 2-fold increase in collagen biosynthesis upon DMBA/TPA treatment (*Methods*) (Fig. 4k and Extended Data Fig. 4b). Mouse dermal fibroblasts also increased collagen biosynthesis, albeit more modestly.

Cells sense mechanical properties of the ECM through specialized transmembrane receptors such as fibrillar collagen-binding integrins [70]. Therefore, we performed a cell-cell communication analysis to evaluate the integrin signalling between pairs of different cell types (*Methods*). Upon DMBA/TPA treatment, in naked mole-rat only the number of epidermal-stromal interactions was significantly increased (Fig. 4n and Extended Data Fig. 4f), which is consistent with an extensive remodelling of the upper dermis.

However, a stromal-immune cell crosstalk can support fibroblast survival upon environmental stress [71,72]. Indeed, we found that in mice, the remodelling of ECM up-regulated immune-activating genes (Fig. 4l and Extended Data Fig. 4c). Following DMBA/TPA treatment, mouse skin greatly increased its population of CAFs, culminating in the highest numbers around the papilloma (Fig. 4b). Immune activation was increased in both dermal fibroblasts and CAFs, which suggested that a pro-inflammatory environment had successfully formed before the macroscopic appearance of tumours (Fig. 4l). Post-treatment, most dermal fibroblasts showed enrichment for the pro-inflammatory iCAF state; following the formation of the papilloma, the CAFs shifted to a myofibroblast state (myCAF), reflecting tumour-driven tissue reorganization (*Methods*) (Fig. 4m). In stark contrast, naked mole-rat fibroblasts suppressed the activity of their immune responses, following DMBA/TPA treatment (Fig. 4l and Extended Data Fig. 4c).

In sum, naked mole-rat skin blocks the formation of a tumour friendly microenvironment by remodelling the ECM while simultaneously suppressing production of inflammatory mediators.

Naked mole-rat fibroblasts lack tumour promoting capabilities

We tested whether naked mole-rat fibroblasts have an intrinsic ability to suppress tumour growth, because it was possible that the absence of T-cell responses alone might mediate tumour resistance. By co-culturing human SCC cells with either naked mole-rat or mouse dermal fibroblasts as three-dimensional (3D) spheres (tumouroids) (Fig. 5a and Extended Data Fig. 5a), all immune cell contributions to tumouroid growth were eliminated. Only cancer cells co-cultured with mouse fibroblasts significantly increased both the tumouroid area and the percentage of cycling cells (Fig. 5b-c).

We found that naked mole-rat fibroblasts also failed to promote tumour growth *in vivo*. We subcutaneously co-injected the fibroblasts with human SCC cells into the flanks of immunodeficient NSG mice, which lack mature T-cells. While tumour growth in the presence of mouse fibroblasts significantly increased, the presence of the naked mole-rat fibroblasts provided no such growth advantage to the cancer cells (Fig. 5d-e). Tumour weight and area were significantly increased only when SCC cells were co-injected with mouse fibroblasts (Fig. 5f and Extended Data Fig. 5b). Tumours were histologically identical regardless of which species fibroblasts were used (Extended Data Fig. 5c). Thus, mouse fibroblasts have intrinsic tumour promoting capabilities not present in naked mole-rat fibroblasts.

To determine how mouse or naked mole-rat fibroblasts affected cancer cell growth *in vivo*, we transcriptionally profiled the human skin tumour xenografts (Fig. 5g). When compared to SCCs

co-injected with mouse fibroblasts, co-injection with naked mole-rat fibroblasts resulted in downregulation of most inflammatory mediators (Fig. 5h-j). Thus, isolated naked mole-rat dermal fibroblasts prevented the activation of inflammation related genes in the tumours (Extended Data Fig. 5d,g,j), similarly to the fibroblast response to DMBA/TPA in skin (Fig. 2q and 4l).

Thus, our data revealed that naked mole-rat fibroblasts have an intrinsic capability to suppress an inflammatory micro-environment during tumour growth (Extended Data Fig. 5d-l).

Discussion

Naked mole-rats can resist skin cancer formation cancer for continuous treatment up to 2 years using the standard DMBA/TPA protocol [9]. We now demonstrate that naked mole-rats can successfully resist even higher concentrations and frequencies of the chemical mutagens for up to six months, similar to the cancer-resistant hairy blind mole-rat [37]. This cancer resistance occurs despite skin cells accumulating the expected mutational landscape and showing hallmarks of physiological stress. To understand the underlying mechanisms used by naked mole-rats to inhibit cancer inception and growth, we compared the single-cell compositional dynamics and transcriptional responses of homeostatic full-thickness naked mole-rat skin with mouse and human, both of which are well-understood model systems. This comparison identified four novel mechanisms by which naked mole-rats successfully resist cancer induction, which together challenge a number of paradigms in skin homeostasis.

First, naked mole-rat skin contains low numbers of resident T-cells, which in mouse and human are integral both to maintaining skin homeostasis and to driving tumorigenesis. In mouse and

human skin, resident T-cells defend against invasive pathogens [43], and aberrant regulation of T-cells contributes to psoriasis, a common chronic inflammatory skin disease, and cancer [43,73]. Similarly, naked mole-rats also recruit T-cells in response to bacterial toxins [9], but in contrast to mouse show no signs of skin inflammation in response to chemically-induced carcinogenesis. Since the direct interaction between T-cells and dermal fibroblasts down-regulates their ECM production [74], the lack of T-cell activation in naked mole-rat skin might explain the ECM divergence between naked mole-rat, human and mouse. The suppression of immune responses in naked mole-rat skin might also, at least in part, explain their selective inflammatory pain insensitivity [75].

Second, naked mole-rat epidermal turnover is accelerated in homeostatic and mutagen treated skin. In mouse, TPA-induced proliferation leads to a 3-fold thickening of epidermis due to sustained hyperplasia with an increase in the number of all nucleated cell layers [76]. The thickening of the epidermis is dramatically less pronounced in naked mole-rats, because the higher progenitor replacement rate is accompanied by accelerated differentiation in the suprabasal layers. Therefore, the naked mole-rat progenitor compartment is rapidly purged of potentially tumorigenic cells; a similar mechanism has been described in thymus [77,78]. Thus, the carcinogenic treatment challenged naked-mole-rat skin, yet its integrity was successfully maintained by better balancing proliferation and differentiation.

Third, we discovered species-specific fibroblast populations that extensively remodelled the ECM in both normal and carcinogen-treated naked mole-rat skin. The current dogma suggests that fibroblast populations in naked mole-rats should promote ageing and tumorigenesis, due to the combination of increased hyaluronic acid, ECM deposition, and production of collagens. The resulting increase in ECM stiffness [79] is normally associated with ageing, the presence of

cancer-associated fibroblasts, and the promotion of tumorigenesis [80]. Paradoxically, naked mole-rats are long-lived and cancer resistant, and we demonstrated that chemical carcinogen treatment does not generate CAFs. This paradox is resolved by understanding the functional differences between naked mole-rat fibroblasts and their mouse counterparts in tissue homeostasis. Specifically, our results indicated that naked mole-rat fibroblasts do not form tumour-promoting niches, both because they fail to upregulate pro-inflammatory mediators found in mouse CAFs and because they lack the pro-tumorigenic interaction with T-cells.

Fourth, naked mole-rat fibroblasts lack intrinsic tumour promoting capabilities, which we directly demonstrated by co-injecting them with human cancer cells. In contrast, similar experiments with mouse fibroblasts enhance tumour formation because the reciprocal signalling between epidermis and dermis creates a cancer-friendly niche [81]. While normal fibroblasts can inhibit cancer cell growth and development, CAFs are key regulators of the tumour's microenvironment through ECM remodelling and crosstalk with infiltrating leukocytes [82-84]. In contrast, naked mole-rat dermal fibroblasts must unidirectionally disrupt this tumour-promoting interaction with cancerous epidermal cells.

Naked mole-rat skin appears to effortlessly resist powerful drug treatments specifically designed to generate aggressive cancers. Our analysis reveals that this cancer resistance rests on multiple interlocking cellular mechanisms that prevent immune responses, escalate cellular turnover, and functionally rewire stromal fibroblasts.

Material and Methods

Animals and tissue samples

All mice were housed in the DKFZ Central Animal Laboratory. Experimental procedures using C57BL/6J mice (Janvier) or NSG mice (Charles River) were performed under the terms and conditions of the experimental animal project licences DKFZ365, G-59/17, G-96/21 and G-351/19 after approval by the local Governmental Ethics Committee. Naked mole-rats were housed at the University of Duisburg-Essen and University of Cambridge. Maintenance of naked mole-rats housed at the University of Duisburg-Essen was approved by the Veterinary Office of the City of Essen (AZ: 32-2-1180-71/328). Tissue sampling from these naked mole-rats was carried out in accordance with the German Regulations for Laboratory Animal Science (GV-SOLAS). Maintenance and skin carcinogenesis treatment of naked mole-rats housed at University of Cambridge were performed under the terms and conditions of the UK Home Office license P7EBFC1B1. Primary skin fibroblasts were obtained from animals housed at the University of Cambridge and experiments carried out under Home Office Licence P7EBFC1B1. All animal experiments conducted in the UK were in accordance with the UK Animals (Scientific Procedures) Act 1986 Amendment Regulations 2012.

Human skin

Formalin-Fixed Paraffin-Embedded (FFPE) skin from the scapular area of a healthy 55-year-old male was purchased from Origene (donor: PA15476B6E) and used for histology and immunofluorescence.

Chemical skin carcinogenesis

Mice and naked mole-rats were treated with one dose of 7,12-dimethylbenz[a]-anthracene (DMBA) followed by repeated application of 12-O-tetradecanoylphorbol 13-acetate (TPA) as

previously described [20]. In brief, shaved backs of female mice were treated once with 100 µg DMBA (Sigma-Aldrich) in 100 µl acetone. After one week, 10 µg TPA (Sigma-Aldrich) in 100 µl acetone was applied three times a week. The mice were sacrificed at the first macroscopic occurrence of papillomas (weeks 10-12). Male naked mole-rats were treated once with 500 µg DMBA (Sigma-Aldrich) in 250 µl acetone. After one week, 60 µg TPA (Sigma-Aldrich) in 250 µl acetone was applied three times a week for 12 or up to 24 weeks. Animals used in this study are listed in Supplementary Table 1.

Single cell isolation

For detailed information about 10X scRNA-sequencing samples see Supplementary Table 2. 1-5 mm^3 biopsies from naked mole-rat or shaved mouse back skin were incubated with either: I) dissociation buffer (1.25 mg/ml collagenase I (Sigma), 0.5 mg/ml collagenase II (Worthington), 0.5 mg/ml collagenase IV (Worthington) and 0.1 mg/ml hyaluronic acid (Sigma) in Hanks Balanced Salt solution (HBSS) (Invitrogen)) for 2.5 hours followed by addition of trypsin (Santa Cruz Biotechnology) to a final concentration of 0.25% for 30 minutes, or II) 0.25% trypsin (Santa Cruz Biotechnology) for 2 hours followed by incubation with dissociation buffer for 1 hour. All dissociation steps were performed at 37°C and shaking at 600 rpm. After 3 hours enzymatic digestion was quenched with HBSS supplemented with 10% fetal bovine serum (FBS, Life Technologies) and cell suspensions filtered through 40 µm cell strainers (Grenier Bio-One). Strainers were washed with an additional 2-3 ml HBSS containing 10% FCS and cells pelleted by centrifugation at 300 x g for 8 minutes at 4°C. Cell pellets were carefully (using wide-bored P1000 pipet tips) resuspended in 100-200 µl sorting buffer (1 mM EDTA (Invitrogen), 0.04% HyClone bovine serum albumin (BSA, GE Healthcare Life Sciences) in PBS). Cell suspensions were either passed through a 40 µm FLOWMI cell strainer (Fisher Scientific) and viability and

concentration determined using 0.4% trypan blue stain (Invitrogen) and Countess II automated cell counter (Invitrogen) or subjected to Fluorescence-activated Cell Sorting (FACS).

515

Cell pellets for FACS were resuspended in sorting buffer containing 1 µg/ml propidium iodide (PI) (Life Technologies) and transferred to low-binding polypropylene FACS tubes. Live cells from each sample were sorted into one 96-well flat-bottom low attachment tissue culture plate well containing 30 µl sorting buffer on a cold plate using Aria II flowcytometry
520 cell sorter (BD Biosciences) with a 70 µm nozzle (70 psi). PI was excited with a 561 nm laser and fluorescence was recorded with a 610/20 595LP filter. Cells were gated using; *i)* FSC-A vs SSC-A to remove debris *ii)* SSC-W vs SSC-A to exclude doublets *iii)* RL780/60-A vs PI-A to exclude auto-fluorescent cells and dead cells (PI positive). Samples were handled on ice whenever possible.

525

Single-cell capturing and library preparation

10X Genomics Chromium Single Cell 3' cDNA libraries were prepared according to the manufactures' instruction. For mouse samples, all sorted cells from one 1 mm^3 biopsy (800-1100 untreated and 2900-5300 DMBA/TPA treated cells) were loaded onto the 10X
530 Chromium Controller. For all other 5 mm^3 biopsy samples (both mouse and naked mole-rat) cell suspensions were diluted to a concentration aiming for recovery of 5000 cells. Briefly, single cells were encapsulated into droplets in the Chromium Controller instrument for cell lysis and barcoded reverse transcription (RT) of mRNA, followed by amplification, shearing and Illumina library construction. Quantification of the libraries was carried out using the
535 Qubit dsDNA HS Assay Kit (Life Technologies), and cDNA integrity was assessed using

D1000 ScreenTapes (Agilent Technologies). Libraries were pooled per species and each pool sequenced on Illumina NovaSeq6000 using either paired-end run sequencing 28 bp on read 1 and 94 bp on read 2 or 100 bp on each read.

540 **Histology and immunofluorescence staining**

Tissues or tumours were fixed overnight with 4% paraformaldehyde (PFA) (Santa Cruz Biotechnology), transferred to 70% ethanol and then embedded into paraffin. Paraffin samples were cut into 5 µm (H&E) or 5-20 µm (RNAscope and immunofluorescence) sections. Paraffin sections were deparaffinized in xylene and rehydrated in a gradient of ethanol and distilled
545 water and stained with haematoxylin and eosin (H&E). For immunofluorescent labelling of paraffin sections, epitopes were retrieved by incubating slides for 20 minutes at 95 °C in 10 mM citrate buffer (pH 6.0) with 0.05% Tween-20. Sections were then blocked for 1 hour with 10% FBS/ 0.1% Triton-X at room temperature (RT). Primary antibodies were diluted in 1% FBS and incubated overnight using the following dilutions: mouse monoclonal KRT14 (1:1000,
550 Abcam, ab7800), rabbit monoclonal KRT10 (1:200, Abcam, ab76318), mouse monoclonal to KRT6 (1:200, Abcam, ab18586), rabbit polyclonal CD3 (1:200, Abcam, ab5690), rabbit polyclonal FSP1/S100A4 (1:100, Abcam, ab41532), rabbit polyclonal Ki67/MKI67 (1:200, Abcam, ab15580). Fluorescence-labelled Alexa Fluor 647- and Alexa Fluor 488-conjugated secondary antibodies (Thermo Fisher Scientific) were added at a dilution of 1:1000 for 1 hour
555 at RT to detect primary antibodies. DAPI 1:3000 (Sigma Aldrich) was used as nuclear counterstain. Slides were mounted using fluorescent mounting media (Agilent).

RNA in situ hybridisation

FFPE blocks of mouse and naked mole-rat skin and spleen fixed in 4% paraformaldehyde and
560 cut into 5 µm (spleen) or 20 µm (skin) sections, were subjected to RNA FISH using the

RNAScope Multiplex Fluorescent Detection Kit V2 Assay (ACDBio, cat. no. 323100) with TSA Vivid Flurophores (Bio-Techne) according to the manufacturers' instructions. Sample pretreatment steps included a 10 min incubation with hydrogen peroxide, a mild target retrieval at 98–102 °C for 15 min and incubation with RNAscope protease plus for 15 min at 40°C. Target probes (*Mm-Cd3d*: 460101-C1; Mm-Krt10: 457901-C2; *Mm-Krt14*: 422521-C3; *Hg-Cd3d*: 1146881-C1; *Hg-Krt10*: 1146891-C2; *Hg-Krt5*: 1168011-C3) were hybridized to the pre-treated sections for 2 hours at 40°C. Sections were counterstained with DAPI (1:5000, Sigma-Aldrich) or WGA (1:50, Invitrogen) and mounted using ProLong Gold Antifade Mountant (ThermoFisher).

Cells and culture conditions

Human squamous carcinoma cells (SCC25, CTR-1628, ATCC) stably expressing GFP and luciferase (SCC25-Luc-GFP) were kindly provided by S.A. Benitah [85]. C57BL/6 mouse embryonic fibroblasts (MEFs) were obtained from ATCC (SCRC-1008), and primary naked mole-rat fibroblasts were isolated as previously described [4].

MEFs and SCC25 were cultured in a humified 37°C incubator with 5% CO_2. Naked mole-rat fibroblasts were grown in a humified 32°C incubator with 5% CO_2 and 3% O_2. SCC25 cells were cultured in DMEM/F12 medium (11320-032, Life Technologies) supplemented with 10% FBS (Life Technologies), 1% Penicillin-Streptomycin (PEST) (Sigma-Aldrich), 400 ng/ml hydrocortisone (Santa Cruz Biotechnology) and 1% Primocin Ant-pm-2 (InVivogen). MEFs and naked mole-rat dermal fibroblasts were cultured in DMEM high glucose (41965-039, Life Technologies) supplemented with 15% FBS (Life Technologies), 1% PEST (Sigma-Aldrich), 1% Sodium pyruvate (Life Technologies), 1% non-essential amino acids (Life Technologies) and 1% Primocin (Ant-pm-2, InVivogen).

For three-dimensional sphere co-culture as tumouroids, SCC25 cells were mixed with mouse or naked mole-rat fibroblasts in a 1:1 ratio in SCC25 media, plated in ultra-low adherent culture dish (Fisher Scientific) and cultured in a humified 37°C incubator with 5% CO_2 for up to 6 days. Fibroblasts were passaged less than 5 times before experiment start. All cells tested negative for mycoplasma infection.

Tumouroid proliferation rate

Spheroids were cultured for 6 days to measure tumouroid growth and proliferation rate. SCC25-Luc-GFP cells co-cultured with mouse or naked mole-rat fibroblasts were incubated with 10 µM 5-ethynyl-2'-deoxyuridine (EdU) (Thermo Fisher) for 1.5 hours. A sample not treated with EdU served as negative control. Tumouroids were gently rinsed with PBS and then fixed with 1% PFA (Santa Cruz) for 15 minutes on ice in the dark. Following fixation, samples were washed in PBS and permeabilised in PBS supplemented with 3% FBS and 0.1% Saponin (Sigma-Aldrich) for 5 minutes at RT. To conjugate EdU to a fluorochrome, an azide-alkyne cycloaddition was performed for 30 minutes at room temperature in the dark. For this, the Click-iT Cell Reaction Buffer Kit (Life Technologies) and 5 µM of Alexa Fluor 647-Azide (Life Technologies) were used. To remove excess reagents and reduce the background signal, the cells were washed twice in PBS supplemented with 3% FBS and 0.1% Saponin. Finally, all samples were resuspended in PBS containing DAPI (1:3000) and imaged using a TCS SP5 II (Leica) confocal microscope.

Celltracker

To measure the viability of the fibroblasts in the tumouroid co-culture, mouse or naked mole-rat fibroblasts were incubated with 10 µm Celltracker fluorescent probes (C34565, Invitrogen)

for 45 minutes at respective growth conditions and then plated together with SCC25-Luc-GFP in ultra-low attachment plates using SCC25-Luc-GFP culture conditions. The presence of fibroblasts in tumoroids was determined after 24 and 48 h by flow cytometry (LSRFortessa analyzer, BD Biosciences). To measure absolute cell numbers, 50 µl of CountBright Absolute Counting beads (C36950, Thermo Fisher) was added to each sample. Data were processed using FlowJo software (version 10.5.3).

Imaging, processing and image analysis

Bright field images were acquired with either a Zeiss Axio Imager M2 Microscope and an Axiocam 506 colour camera or Zeiss Axioscan 7 using Zen (version 2.6) software (Carl Zeiss). Fluorescence microscopy images were acquired with either LSM 700 (Carl Zeiss) confocal microscope using Zen software or Zeiss Axioscan7 using Zen (version 2.6) software (Carl Zeiss). All images were further processed using Fiji software. All measurements were performed either blinded for condition or by semi-automated macros.

Co-injection xenograft model

One million SCC25-GFP-Luc cells were mixed with i) one million mouse fibroblasts (MEFs), ii) one million naked mole-rat fibroblasts, or iii) no fibroblasts. Viability of cells was higher than 95%. Cell mixtures were diluted in PBS and kept on ice up until injection. 100 µl of cell mixtures were injected subcutaneously using a 22-gauge needle to both flanks of 8-weeks old female immunosuppressed NSG mice (N = 5-6 per experimental group *i-iii*). Mice were anaesthetized using isofluorane gas during injection procedure. Tumour growth was monitored for 28 days by measuring the luciferase bioluminescent signal (BLI) using the IVIS Lumina III In Vivo Imaging System (Perkin Elmer). For this, mice received intraperitoneal injection of 50 µl 30 mg/ml d-luciferin (in PBS) (E1603, Promega). Continuous administration of isofluorane

gas was provided to maintain anaesthesia of animals during imaging. Data were quantified with Living Image software version 4.7 (Perkin Elmer). Regions of interest were drawn manually and BLI signal was quantified as total photon flux (photons/second). Colour scale for minimum and maximum values of the BLI are shown in the images.

DNA isolation from skin biopsies and livers

DNA was isolated from 1 mm^3 mouse and naked mole-rat back skin biopsies and livers using a modified and combined version of the AllPrep DNA/RNA Micro Kit (Qiagen) and DNeasy Blood and Tissue Kit (Qiagen). Briefly, 350 µl RLT buffer (from the AllPrep DNA/RNA Micro Kit) containing 1% β-Mercaptoethanol (Sigma-Aldrich) was added to each sample (containing one biopsy) and the tissue was homogenised in a Qiagen TissueLyzer II using 2 cycles of 3 minutes at 30 Hz. After lysis 688 µl of nuclease-free water and 12 µl proteinase K (from DNeasy Blood and Tissue Kit) was added to the lysate and incubated at 56°C for 10 minutes. Half of the sample (519 ul) was used for DNA extraction. 519 µl Buffer AL (Qiagen Blood & Tissue) was added, mix by vortexing, and incubated at 56°C for 30 minutes at 500 rpm. An equal volume (519 µl) of absolute ethanol was added to samples and mixed thoroughly. The precipitated mixture was transferred to a DNeasy Mini spin 96-well spin plate (Qiagen), washed twice with 700 µl buffer AW1 and twice with buffer AW2. After drying the membrane for 3 minutes at 20,000 x g DNA was eluted using two consecutive elutions of 30 µl pre-warmed AE buffer (70°C). The quality of the DNA was assessed using a Genomic DNA ScreenTape (Agilent Technologies).

Whole-exome sequencing

Dual indexed whole exome capture libraries were prepared from mouse and naked mole-rat skin biopsies and matched livers using SureSelect XT HS and XT Low Input Enzymatic

Fragmentation protocol (Agilent). For mouse whole exome sequencing (WES) libraries SureSelectXT Low Input Target Enrichment System was used with Mouse All Exon capture kit (49.6 Mb). For naked mole-rat WES libraries SureSelectXT HS / SureSelectXT Low Input Target Enrichment with Pre-Capture Pooling was used with a custom-designed NMR all exon capture array (Agilent). Exome libraries were sequenced on Illumina NextSeq2000 and NovaSeq6000 sequencers using a 100 bp paired-end read protocol.

RNA-sequencing of xenografted tumours

SCC25 tumours from the co-injection experiment were dissected at day 28 and homogenized in lysis buffer from the Qiagen AllPrep mini kit using Tissue Lyzer II (Qiagen). Total RNA was isolated using Qiagen AllPrep mini kit (Qiagen) and DNase digested (AM1907, Invitrogen) according to manufacturers' instructions. RNA concentration was measured using a NanoDrop spectrophotometer (Thermo Fisher): RNA integrity was assessed using RNA ScreenTapes (Agilent Technologies). The RNA integrity number (RIN) was above 8.6 for all samples. 100 ng DNase treated RNA was used to generate ribo-minus treated total RNA stranded libraries using Illumina Stranded Total RNA Prep Ligation with Ribo-Zero Plus kit (Illumina) according to manufactures' instructions. Pooled libraries were sequenced on a Illumina NextSeq2000 using a P3 flow cell to produce 100 bp pair-end reads.

Single-cell cell-type annotation

The droplet-based sequencing data were aligned using the Cell Ranger Single-Cell Software Suite (v. 3.0.1, 10x Genomics) against the GRCm38 (mm10) and HetGla female 1.0 mouse and naked mole-rat references, respectively. Cells with fewer than 600 detected genes; greater than 10% mitochondrial reads; or log10 total mRNA counts greater than two standard deviations from average across all cells (per species) were removed.

In the single-species analyses (SS), expression was first normalised using SCtransform [86] regressing out the percentage of mitochondrial genes within each biopsy. The different biopsies were then integrated using the canonical correlation analysis and mutual nearest neighbour approach implemented in the Seurat R package [87], using the 3000 most variable features. Doublets were identified separately in each species using the function doubletCells from the scran package (Bioconductor) [88]. Cells with a log10 score + 1 greater than 4 were removed. Louvain clusters were determined with resolution parameter 0.5 and cluster markers were determined with the FindAllMarkers Seurat function using default parameters.

For the 3-species integration (INT) analyses, the count matrices were first subset to one-to-one-to-one orthologue genes. Individual biopsies from all 3 species were integrated together using the Seurat rPCA approach using the biopsies with the largest number of cells from each species and each treatment as the reference set. Clusters and markers were determined as above.

The annotation of the high-level cell-types (T-cells, APCs, epithelial, fibroblasts, endothelial, muscle, melanocytes, mast and Schwann cells, see Figure 1) was done in four steps: first, separately for each species, we manually assigned cell-types based on the cluster markers (the SS approach described above). Second, we integrated the three species and manually assigned cell-types based on the cluster markers (the INT approach described above). Third, for a minority (5.4%) of naked mole-rat cells, the SS and INT annotations yielded different results. To break the tie for these ambiguous cells, we generated a 3rd annotation using Garnett with the following markers: fibroblasts - DCN, COL1A1, LUM; epithelial - KRT5, KRT14, KRT1, KRT10; APCs - CD74, CD207, CD83, LYZ; T-cells - (subtype of APCs): CD3D, CD3E, CD3G; endothelial - SELE, PVAP; muscle - MYL1, CKM, MYOD1, DES; melanocytes -

PMEL, MLANA; Schwann - DRP2, KCNA1, PMP22, PLP1, SCNA; mast - CMA1, CPA3. Finally, for these ambiguous cells, we built a neural network to generate a 4th annotation. For each cell, the final annotation was picked as the consensus of all four methods. Cells for which there was no consensus (2.9% of all cells) were excluded. For the sub-clustering of the epithelial compartments we isolated the epithelial cells and re-ran the Louvain clustering with resolution parameter 0.5. Cluster identities were manually assigned using the markers in Supplementary Table 3. For the sub-clustering of stromal cells, we isolated these cells and re-ran the Louvain clustering with resolution parameters 0.25, 0.5 and 1. Cluster identities were manually assigned using the markers in Supplementary Table 3.

Differential expression, gene set enrichment and over-representation analyses

To perform the differential expression analysis of untreated samples between species we summed up the counts over all cells within each biopsy and cell-type (epithelial, fibroblasts, APCs and T-cells) to create pseudo-bulk expression profiles. The pseudo-bulk expression profiles of the three species were normalized together (using 1:1:1 orthologue genes), and pairwise differential expression was performed using the DESeq2 R/Bioconductor package [89], with default parameters. P values were adjusted for multiple testing using Benjamini-Hochberg's method.

For gene set enrichment analyses we used the weighted approach implemented in GSEA [47]. For the over-representation analysis, we restricted the analysis to autosomal genes that were: i) significantly differentially expressed (Benjamini-Hochberg adjusted P-value < 0.05) between naked mole-rat and human; ii) significantly differentially expressed between naked mole-rat and mouse; and iii) with fold changes in the same direction in the two species comparisons. We then used a hypergeometric distribution to test for enrichment of gene sets in the GO

Biological Process, Reactome, WikiPathways, KEGG and MSigD/B Hallmarks databases [90] over the background of all expressed orthologous genes (genes with at least 1 count in our experiments). P values were adjusted for multiple testing of gene sets using Benjamini-Hochberg's method.

For the differential expression analyses between untreated and treated samples, we used the same pseudo-bulk approach described above, summing up read counts from all epithelial, fibroblasts, APC and T-cells within each replicate prior to differential expression testing using DEseq2. Genes were only included in this analysis if they were expressed (defined as having at least 2 counts) in at least 10% of all cells. Note that the number of replicates in each condition is the same for all cell types as they are subsets of cells from the same experiments.

Cell type proportions

To test for changes in the proportion of epithelial (Fig. 3h) and fibroblasts (Fig. 4b) cell types upon treatment, we calculated the proportion of each cell type in each biopsy and applied a centred log ratio (CLR) transformation. This was used as input for a linear model in which different cell type CLR values were used to predict if the biopsy had undergone DMBA/TPA treatment or not. P values were calculated from the t statistics associated with the slope of each cell type.

DMBA mutational burden analysis

To identify a DMBA signature, we performed whole exome sequencing on 6 mouse biopsies treated with DMBA/TPA, 6 untreated mouse biopsies, 4 naked mole-rat biopsies treated with DMBA/TPA, 3 naked mole-rat biopsies treated with TPA only, and 1 untreated naked mole-rat biopsy. Reads were trimmed with Trim Galore and mapped to the mouse or naked mole-rat

reference genome using bwa mem. Different lanes from the same sample were merged and duplicate reads removed with gatk MarkDuplicates [91]. Somatic mutations were called on the DMBA-treated samples using GATK Mutect2 with liver samples from the same animal used as a matched normal. Somatic variants with a sequencing coverage below 30 were filtered out and excluded from downstream analyses. The remaining somatic variants were used to calculate the fraction of mutations at each of the 96 possible trinucleotide contexts. Using non-negative matrix factorization, we extracted 5 mutational signatures. One signature closely resembled the DMBA signature reported in the literature of a strong preference for T>A transversions in a C.G, G.G and T.G context [21]. We used this signature as the reference DMBA signature. To ascertain that the reference DMBA mutational signature was present in the skin samples, we subtracted the mutational frequency of the control samples from the treated samples and calculated the treated sample cosine similarity to the reference DMBA signature.

Progenitor replacement rate

Assuming neutral competition, the probability P of finding a clone of size n progenitors is given by the following equation [61]:

$$P_n = \frac{1}{\ln(r\lambda)} \frac{e^{-\frac{n}{r\lambda}}}{n}$$

where $r\lambda$ is the loss/replacement rate of the basal progenitor cells. This equation can be manipulated by calculating the first incomplete moment μ of the clone size distribution, defined as:

$$\mu(n) = \frac{1}{\langle n \rangle} \sum_{m=n}^{\infty} m P_m$$

where $\langle n \rangle$ is the average clone size in a biopsy. If the dynamics of cell loss and replacement follow neutral assumptions, the first incomplete moment assumes an exponential distribution:

$$\mu(n) = e^{-\frac{n}{r\lambda}}$$

with the corresponding distribution of clone areas A given by

$$\mu(A) = e^{-\frac{\rho A}{r\lambda}} = e^{-\frac{A}{k}}$$

The clone areas are proportional to the biopsy size (1 mm^2) and the variant allele frequency (VAF) associated with the individual single nucleotide variant that defines the clone. Very few mutations involve a change in copy number, so the areal contribution of individual mutant clones can be approximated as twice the VAF.

The first incomplete moment of cell populations under drift will follow an exponential distribution, so plotting the logarithm of the incomplete moment versus clone area will result in straight lines. For biopsies in which this was observed, the progenitor replacement rate was estimated by fitting the exponent $\frac{\rho}{r\lambda}$ to the incomplete moment distribution.

Single-cell trajectory analysis of interfollicular epithelial cells

An epithelial cell differentiation trajectory was calculated using Monocle3 on the Seurat-generated UMAP. Its starting point was selected based on the interfollicular epithelial cells containing the highest expression of the undifferentiated basal marker genes KRT14, COL17A1, ITGA6, THY1.

Gene set and cell-cycle scoring

To identify cells with active gene scores, AUCell [92] was used to calculate the "Area Under the Curve" for the following gene sets: Fibroblast migration (GO:0010761), Collagen biosynthetic process (GO:0032964), Activation of immune response (GO:0002253). Dermal location gene sets for fibroblast 1-6 were generated from previously reported marker genes in human skin [29,93-96] and 7-15 from previously reported marker genes in mouse skin [31] (excluding overlapping genes between FIB-1-2 and 3-4). Previously reported gene signatures were used

to classify myofibroblast CAF (myCAF) or pro-inflammatory CAF (iCAF) states [97,98]. For full gene set tables for dermal location and CAFs see Supplementary Table 4. We used an unpaired t-test to find statistical differences in the mean scores of each untreated biopsy versus each DMBA/TPA treated biopsy.

815

To classify the cell cycle phase of epithelial cells a score was assigned to each cell based on its expression of G2/M and S phase markers using the CellCycleScoring function in the Seurat package in R [99,100].

820 **Cell-cell communication**

To study how different cell types communicate, the 'method statistical_analysis' command from CellPhoneDB [101] (https://github.com/Teichlab/cellphonedb) was run with default parameters for each species (mouse and naked mole-rat) and treatment (UN and DT) separately, using the raw counts. Cell types were annotated by their lower level annotations
825 from the epidermal and fibroblast sub-clusterings.

To estimate the prevalence of integrin-mediated communication between cells in each species and each condition, we discarded i) cell type pairs involving a cell type for which fewer than 10 cells were identified, ii) cell type pairs for which fewer than 10 significant (raw P value <
830 0.05) molecular interactions were identified, iv) cell type pairs which were not found across both conditions being compared (e.g. both treatments within the same species). For the remaining cell type pairs, we calculated the percentage of significant molecular interactions involving integrin. For each species, we calculated the difference in the percentage of integrin-mediated interactions upon treatment. Cell types were aggregated into their higher level
835 annotation (epithelial, fibroblast and APCs) for their display in boxplots.

To compare all types of cell-cell communication upon treatment (not exclusively integrin-mediated interactions), we filtered cell type pairs as above. We then ranked them according to the number of significant (raw P value < 0.05) molecular interactions identified between them
840 before and after treatment. A decrease (or increase) in rank upon treatment could indicate a decrease (or increase) in the amount of communication occurring between two cell types. Multiple such changes (i.e. a wide distribution of rank changes) could indicate a general rearrangement in how cells communicate within the tissue. Conversely, few changes (i.e. a narrow distribution of rank changes) could be indicative of cell-cell communication not being
845 impacted by the treatment. To compare the amount of such rearrangement across both species, we calculated the change in rank for every cell type pair and normalised this by the total number of ranks in each species (resulting in a number ranging from -1 to 1). We used the var.test function in R to implement an F-test and compare the variances in the normalized rank difference distributions between both species.

850

To study cell-cell communication (all interactions, or only exclusively integrin-mediated) between Fibroblasts I-VI, we calculated the percentage of significant interactions between each pair of cell types in untreated biopsies and in biopsies treated with DMBA/TPA. We then calculated the log ratio of the number of significant interactions in DMBA/TPA-treated
855 biopsies over the number of significant interactions in untreated biopsies. To calculate a *P* value for the change in cell-cell communication upon treatment, we performed Fisher's exact tests.

RNA-seq data processing and analysis of SCC tumours

We extracted the raw number of reads mapping to each gene (DKFZ/ODCF pipeline, see above) in the RNAseq data derived from each of the tumour co-injection experiments (tumour alone, tumour co-injected with mouse fibroblasts, tumour co-injected with naked mole-rat fibroblasts). These counts were used as input for a differential gene expression analysis (performed using the 'DESeq' function from the 'deseq2' package in R). For each gene in each condition, this estimates a normalized gene expression metric (median of ratios) [89] as well as a dispersion metric. A principal components analysis was performed using the median of ratios of the 500 most variable genes in the dataset. Components 2, 3 and 4 were visualized with the 'plot3d' function of the 'rgl' package in R. The 'results' function from the 'deseq2' package was used to perform differential gene expression analyses across all three pairwise combinations of tumour co-injection experiments.

Statistical analyses and reproducibility

All plots were created using R/4.0.0 or Prism 9 software.

Graphical illustrations

Mice and naked mole-rat illustrations were created by Angela Goncalves. All other illustrations were generated using BioRender.

Data availability

Mouse and naked mole-rat single-cell RNA-seq datasets (10X Chromium) are available from ArrayExpress accession number E-MTAB-12451; E-MTAB-12454; E-MTAB-12456; E-MTAB-12459; E-MTAB-12461. Bulk RNA-seq datasets of co-injected naked mole-rat and mouse fibroblasts with SCCs into host mice are available from ArrayExpress under the accession number E-MTAB-12455. Mouse and naked mole-rat WES datasets are submitted to the Sequencing Read Archive (SRA) under the accession number PRJNA903661. Human single cell RNA-seq dataset is available from the Gene Expression Omnibus (GEO) database under the accession number GSE130973.

Acknowledgments

We especially thank Hayley Forest, Alexandra Robinson, Gemini Chu (Combined Animal Facility Cambridge, University of Cambridge) and Michael Webb and Sarah Elderkin (Cancer Research UK Cambridge Institute) for their invaluable support with the naked mole-rat skin carcinogenesis experiment. We thank all DKFZ core facilities for their support, and in particular Damir Kunic and colleagues at the light microscopy facility. Special thanks also go to Karin Müller-Decker for her support with the animal experiments, and Frank Lyko for providing single cell sequencing data. We also thank all members of staff of the DKFZ Central Animal Laboratory for their support. We thank Prof. Dr. Jürgen Becker and team members from the University of Duisburg-Essen, Faculty of Biology, for support with 10X Chromium. We thank Vladimir Botchkarev and Andrei Mardaryev for providing naked mole-rat tissue for training purposes; no data from these tissues was used in this study. This work was funded by the Helmholtz Association. MB was supported by international postdoc fellowship from the Swedish Research Council (2017-06173) and Marie Skłodowska-Curie individual fellowship (896324). This work was supported by NCT/Helmholtz core funding (A350 to MF, B270 to

D.T.O., B210 to A.G.); European Research Council (788937 to D.T.O.); Wellcome Investigator award (202878/Z/16/Z to DTO), Helmholtz junior group leader award (to A.G.). Dunhill Medical Trust (RPGF2002\188 to E.St.J.S.).

910 **Author contributions**

AG, MF, DTO, MB: designed experiments and wrote manuscript.

MB, SD: performed experiments

PBC, AG, MB, MF, LPD, NH, FJBB: analysed data.

MB, MK, SDP, DS, MS, CR, JD: collected and processed tissue samples.

915 FL: curated data and provided data management.

SB, ESJ, WTK: provided naked mole-rat tissues or cells.

LSB: provided human skin single cell RNA sequencing data.

Declaration of interests

920 All authors declare no conflict of interest.

References

1 Buffenstein, R. *et al.* The naked truth: a comprehensive clarification and classification of current 'myths' in naked mole-rat biology. *Biol Rev Camb Philos Soc* **97**, 115-140 (2022). https://doi.org:10.1111/brv.12791

2 Hadi, F., Smith, E. S. J. & Khaled, W. T. Naked Mole-Rats: Resistant to Developing Cancer or Good at Avoiding It? *Extraordinary Biology of the Naked Mole-Rat* **1319**, 341-352 (2021). https://doi.org:10.1007/978-3-030-65943-1_14

3 Zhao, J. *et al.* Reply to: Transformation of naked mole-rat cells. *Nature* **583**, E8-E13 (2020). https://doi.org:10.1038/s41586-020-2411-9

4 Hadi, F. *et al.* Transformation of naked mole-rat cells. *Nature* **583**, E1-+ (2020). https://doi.org:10.1038/s41586-020-2410-x

5 Delaney, M. A., Nagy, L., Kinsel, M. J. & Treuting, P. M. Spontaneous histologic lesions of the adult naked mole rat (Heterocephalus glaber): a retrospective survey of lesions in a zoo population. *Vet Pathol* **50**, 607-621 (2013). https://doi.org:10.1177/0300985812471543

6 Delaney, M. A. *et al.* Initial Case Reports of Cancer in Naked Mole-rats (Heterocephalus glaber). *Veterinary Pathology* **53**, 691-696 (2016). https://doi.org:10.1177/0300985816630796

7 Taylor, K. R., Milone, N. A. & Rodriguez, C. E. Four Cases of Spontaneous Neoplasia in the Naked Mole-Rat (Heterocephalus glaber), A Putative Cancer-Resistant Species. *J Gerontol a-Biol* **72**, 38-43 (2017). https://doi.org:10.1093/gerona/glw047

8 Cole, J. E., Steeil, J. C., Sarro, S. J., Kerns, K. L. & Cartoceti, A. Chordoma of the sacrum of an adult naked mole-rat. *J Vet Diagn Invest* **32**, 132-135 (2020). https://doi.org:Artn 1040638719894985 10.1177/1040638719894985

9 Oka, K. *et al.* Resistance to chemical carcinogenesis induction via a dampened inflammatory response in naked mole-rats. *Commun Biol* **5**, 287 (2022). https://doi.org:10.1038/s42003-022-03241-y

10 Kim, E. B. *et al.* Genome sequencing reveals insights into physiology and longevity of the naked mole rat. *Nature* **479**, 223-227 (2011). https://doi.org:10.1038/nature10533

11 MacRae, S. L. *et al.* DNA repair in species with extreme lifespan differences. *Aging-Us* **7**, 1171-1184 (2015). https://doi.org:DOI 10.18632/aging.100866

12 Tian, X. *et al.* INK4 locus of the tumor-resistant rodent, the naked mole rat, expresses a functional p15/p16 hybrid isoform. *Proceedings of the National Academy of Sciences of the United States of America* **112**, 1053-1058 (2015). https://doi.org:10.1073/pnas.1418203112

13 Tian, X. *et al.* High-molecular-mass hyaluronan mediates the cancer resistance of the naked mole rat. *Nature* **499**, 346-U122 (2013). https://doi.org:10.1038/nature12234

14 Miyawaki, S. *et al.* Tumour resistance in induced pluripotent stem cells derived from naked mole-rats. *Nature communications* **7** (2016). https://doi.org:ARTN 11471 10.1038/ncomms11471

15 Urriola-Muñoz, P., Pattison, L.A., St. John Smith, E. Dysregulation of ADAM10 shedding activity as a mechanism of cancer resistance in the naked mole-rat. *bioRxiv* **https://doi.org/10.1101/2022.06.09.495538** (2022).

16 Cagan, A. *et al.* Somatic mutation rates scale with lifespan across mammals. *Nature* **604**, 517-524 (2022). https://doi.org:10.1038/s41586-022-04618-z

17 Sung, H. *et al.* Global Cancer Statistics 2020: GLOBOCAN Estimates of Incidence and Mortality Worldwide for 36 Cancers in 185 Countries. *CA Cancer J Clin* **71**, 209-249 (2021). https://doi.org:10.3322/caac.21660

18 Que, S. K. T., Zwald, F. O. & Schmults, C. D. Cutaneous squamous cell carcinoma: Incidence, risk factors, diagnosis, and staging. *J Am Acad Dermatol* **78**, 237-247 (2018). https://doi.org:10.1016/j.jaad.2017.08.059

19 Gober, M. D., Bashir, H. M. & Seykora, J. T. Reconstructing skin cancers using animal models. *Cancer Metast Rev* **32**, 123-128 (2013). https://doi.org:10.1007/s10555-012-9410-8

20 Abel, E. L., Angel, J. M., Kiguchi, K. & DiGiovanni, J. Multi-stage chemical carcinogenesis in mouse skin: fundamentals and applications. *Nat Protoc* **4**, 1350-1362 (2009). https://doi.org:10.1038/nprot.2009.120

21 Nassar, D., Latil, M., Boeckx, B., Lambrechts, D. & Blanpain, C. Genomic landscape of carcinogen-induced and genetically induced mouse skin squamous cell carcinoma. *Nat Med* **21**, 946-954 (2015). https://doi.org:10.1038/nm.3878

22 Balmain, A., Ramsden, M., Bowden, G. T. & Smith, J. Activation of the mouse cellular Harvey-ras gene in chemically induced benign skin papillomas. *Nature* **307**, 658-660 (1984). https://doi.org:10.1038/307658a0

23 Quintanilla, M., Brown, K., Ramsden, M. & Balmain, A. Carcinogen-specific mutation and amplification of Ha-ras during mouse skin carcinogenesis. *Nature* **322**, 78-80 (1986). https://doi.org:10.1038/322078a0

24 Bizub, D., Wood, A. W. & Skalka, A. M. Mutagenesis of the Ha-ras oncogene in mouse skin tumors induced by polycyclic aromatic hydrocarbons. *Proc Natl Acad Sci U S A* **83**, 6048-6052 (1986). https://doi.org:10.1073/pnas.83.16.6048

25 Su, F. *et al.* RAS mutations in cutaneous squamous-cell carcinomas in patients treated with BRAF inhibitors. *N Engl J Med* **366**, 207-215 (2012). https://doi.org:10.1056/NEJMoa1105358

26 Seluanov, A., Gladyshev, V. N., Vijg, J. & Gorbunova, V. Mechanisms of cancer resistance in long-lived mammals. *Nature Reviews Cancer* **18**, 433-441 (2018). https://doi.org:10.1038/s41568-018-0004-9

27 Bragulla, H. H. & Homberger, D. G. Structure and functions of keratin proteins in simple, stratified, keratinized and cornified epithelia. *J Anat* **214**, 516-559 (2009). https://doi.org:10.1111/j.1469-7580.2009.01066.x

28 Zhang, X., Yin, M. & Zhang, L. J. Keratin 6, 16 and 17-Critical Barrier Alarmin Molecules in Skin Wounds and Psoriasis. *Cells* **8** (2019). https://doi.org:10.3390/cells8080807

29 Sole-Boldo, L. *et al.* Single-cell transcriptomes of the human skin reveal age-related loss of fibroblast priming. *Commun Biol* **3**, 188 (2020). https://doi.org:10.1038/s42003-020-0922-4

30 Savina, A. *et al.* Single-cell transcriptomics reveals age-resistant maintenance of cell identities, stem cell compartments and differentiation trajectories in long-lived naked mole-rats skin. *Aging* **14**, 3728-3756 (2022). https://doi.org:10.18632/aging.204054

31 Joost, S. *et al.* The Molecular Anatomy of Mouse Skin during Hair Growth and Rest. *Cell Stem Cell* **26**, 441-457 e447 (2020). https://doi.org:10.1016/j.stem.2020.01.012

32 Reynolds, G. *et al.* Developmental cell programs are co-opted in inflammatory skin disease. *Science* **371** (2021). https://doi.org:10.1126/science.aba6500

33 Hao, Y. *et al.* Integrated analysis of multimodal single-cell data. *Cell* **184**, 3573-3587 e3529 (2021). https://doi.org:10.1016/j.cell.2021.04.048
34 Hilton, H. G. *et al.* Single-cell transcriptomics of the naked mole-rat reveals unexpected features of mammalian immunity. *PLoS Biol* **17**, e3000528 (2019). https://doi.org:10.1371/journal.pbio.3000528
35 Harjunpaa, H., Asens, M. L., Guenther, C. & Fagerholm, S. C. Cell Adhesion Molecules and Their Roles and Regulation in the Immune and Tumor Microenvironment. *Frontiers in Immunology* **10** (2019). https://doi.org:ARTN 1078
10.3389/fimmu.2019.01078
36 Dunlevy, J. R. & Couchman, J. R. Interleukin-8 induces motile behavior and loss of focal adhesions in primary fibroblasts. *J Cell Sci* **108 (Pt 1)**, 311-321 (1995). https://doi.org:10.1242/jcs.108.1.311
37 Manov, I. *et al.* Pronounced cancer resistance in a subterranean rodent, the blind mole-rat, Spalax: in vivo and in vitro evidence. *BMC Biol* **11**, 91 (2013). https://doi.org:10.1186/1741-7007-11-91
38 McCreery, M. Q. *et al.* Evolution of metastasis revealed by mutational landscapes of chemically induced skin cancers. *Nat Med* **21**, 1514-1520 (2015). https://doi.org:10.1038/nm.3979
39 Goel, G., Makkar, H. P., Francis, G. & Becker, K. Phorbol esters: structure, biological activity, and toxicity in animals. *Int J Toxicol* **26**, 279-288 (2007). https://doi.org:10.1080/10915810701464641
40 Mochly-Rosen, D., Das, K. & Grimes, K. V. Protein kinase C, an elusive therapeutic target? *Nat Rev Drug Discov* **11**, 937-957 (2012). https://doi.org:10.1038/nrd3871
41 Girardi, M. *et al.* The distinct contributions of murine T cell receptor (TCR)gammadelta+ and TCRalphabeta+ T cells to different stages of chemically induced skin cancer. *J Exp Med* **198**, 747-755 (2003). https://doi.org:10.1084/jem.20021282
42 Clark, R. A. *et al.* The vast majority of CLA+ T cells are resident in normal skin. *J Immunol* **176**, 4431-4439 (2006). https://doi.org:10.4049/jimmunol.176.7.4431
43 Tokura, Y., Phadungsaksawasdi, P., Kurihara, K., Fujiyama, T. & Honda, T. Pathophysiology of Skin Resident Memory T Cells. *Front Immunol* **11**, 618897 (2020). https://doi.org:10.3389/fimmu.2020.618897
44 Watanabe, R. *et al.* Human skin is protected by four functionally and phenotypically discrete populations of resident and recirculating memory T cells. *Science translational medicine* **7** (2015). https://doi.org:ARTN 279ra39
10.1126/scitranslmed.3010302
45 Squair, J. W., Skinnider, M. A., Gautier, M., Foster, L. J. & Courtine, G. Prioritization of cell types responsive to biological perturbations in single-cell data with Augur. *Nat Protoc* **16**, 3836-3873 (2021). https://doi.org:10.1038/s41596-021-00561-x
46 Mootha, V. K. *et al.* PGC-1alpha-responsive genes involved in oxidative phosphorylation are coordinately downregulated in human diabetes. *Nat Genet* **34**, 267-273 (2003). https://doi.org:10.1038/ng1180
47 Subramanian, A. *et al.* Gene set enrichment analysis: a knowledge-based approach for interpreting genome-wide expression profiles. *Proc Natl Acad Sci U S A* **102**, 15545-15550 (2005). https://doi.org:10.1073/pnas.0506580102
48 Lin, C. C. *et al.* Bhlhe40 controls cytokine production by T cells and is essential for pathogenicity in autoimmune neuroinflammation. *Nat Commun* **5**, 3551 (2014). https://doi.org:10.1038/ncomms4551
49 Salmon, A. J. *et al.* BHLHE40 Regulates the T-Cell Effector Function Required for Tumor Microenvironment Remodeling and Immune Checkpoint Therapy Efficacy. *Cancer Immunol Res* **10**, 597-611 (2022). https://doi.org:10.1158/2326-6066.CIR-21-0129
50 Bailey, S. R. *et al.* Th17 cells in cancer: the ultimate identity crisis. *Front Immunol* **5**, 276 (2014). https://doi.org:10.3389/fimmu.2014.00276
51 Papanicolaou, M. *et al.* Temporal profiling of the breast tumour microenvironment reveals collagen XII as a driver of metastasis. *Nat Commun* **13**, 4587 (2022). https://doi.org:10.1038/s41467-022-32255-7
52 Tanaka, M. & Siemann, D. W. Gas6/Axl Signaling Pathway in the Tumor Immune Microenvironment. *Cancers (Basel)* **12** (2020). https://doi.org:10.3390/cancers12071850
53 Chan, I. The role of extracellular matrix protein 1 in human skin. *Clin Exp Dermatol* **29**, 52-56 (2004). https://doi.org:DOI 10.1111/j.1365-2230.2004.01440.x
54 Demeter, M., Derenyi, I. & Szollosi, G. J. Trade-off between reducing mutational accumulation and increasing commitment to differentiation determines tissue organization. *Nature communications* **13** (2022). https://doi.org:ARTN 1666
10.1038/s41467-022-29004-1
55 Lin, Z. G. *et al.* Murine interfollicular epidermal differentiation is gradualistic with GRHL3 controlling progression from stem to transition cell states. *Nature communications* **11** (2020). https://doi.org:ARTN 5434
10.1038/s41467-020-19234-6
56 Wang, S. *et al.* Single cell transcriptomics of human epidermis identifies basal stem cell transition states. *Nat Commun* **11**, 4239 (2020). https://doi.org:10.1038/s41467-020-18075-7
57 Dekoninck, S. *et al.* Defining the Design Principles of Skin Epidermis Postnatal Growth. *Cell* **181**, 604-620 e622 (2020). https://doi.org:10.1016/j.cell.2020.03.015
58 Aragona, M. *et al.* Mechanisms of stretch-mediated skin expansion at single-cell resolution. *Nature* **584**, 268-+ (2020). https://doi.org:10.1038/s41586-020-2555-7
59 Cockburn, K. *et al.* Gradual differentiation uncoupled from cell cycle exit generates heterogeneity in the epidermal stem cell layer. *Nat Cell Biol* (2022). https://doi.org:10.1038/s41556-022-01021-8
60 Cohen, E., Johnson, C., Redmond C.J., Nair R.R., Coulombe, P.A. . Revisiting the significance of keratin expression in complex epithelia. *bioRxiv* (2022).
61 Simons, B. D. Deep sequencing as a probe of normal stem cell fate and preneoplasia in human epidermis. *Proceedings of the National Academy of Sciences of the United States of America* **113**, 128-133 (2016). https://doi.org:10.1073/pnas.1516123113
62 Roberts, K. J., Kershner, A. M. & Beachy, P. A. The Stromal Niche for Epithelial Stem Cells: A Template for Regeneration and a Brake on Malignancy. *Cancer cell* **32**, 404-410 (2017). https://doi.org:10.1016/j.ccell.2017.08.007
63 Zhang, J., Chen, L., Xiao, M., Wang, C. & Qin, Z. FSP1+ fibroblasts promote skin carcinogenesis by maintaining MCP-1-mediated macrophage infiltration and chronic inflammation. *Am J Pathol* **178**, 382-390 (2011). https://doi.org:10.1016/j.ajpath.2010.11.017
64 Biggs, L. C. *et al.* Hair follicle dermal condensation forms via Fgf20 primed cell cycle exit, cell motility, and aggregation. *eLife* **7** (2018). https://doi.org:10.7554/eLife.36468

65 Ahlers, J. M. D. *et al.* Single-Cell RNA Profiling of Human Skin Reveals Age-Related Loss of Dermal Sheath Cells and Their Contribution to a Juvenile Phenotype. *Frontiers in genetics* **12** (2022). https://doi.org:ARTN 797747 10.3389/fgene.2021.797747
66 Lavie, D., Ben-Shmuel, A., Erez, N. & Scherz-Shouval, R. Cancer-associated fibroblasts in the single-cell era. *Nat Cancer* **3**, 793-807 (2022). https://doi.org:10.1038/s43018-022-00411-z
67 Thompson, S. M., Phan, Q. M., Winuthayanon, S., Driskell, I. M. & Driskell, R. R. Parallel Single-Cell Multiomics Analysis of Neonatal Skin Reveals the Transitional Fibroblast States that Restrict Differentiation into Distinct Fates. *J Invest Dermatol* **142**, 1812-+ (2022). https://doi.org:10.1016/j.jid.2021.11.032
68 Efremova, M., Vento-Tormo, M., Teichmann, S. A. & Vento-Tormo, R. CellPhoneDB: inferring cell-cell communication from combined expression of multi-subunit ligand-receptor complexes. *Nat Protoc* **15**, 1484-1506 (2020). https://doi.org:10.1038/s41596-020-0292-x
69 Sun, B. The mechanics of fibrillar collagen extracellular matrix. *Cell Rep Phys Sci* **2** (2021). https://doi.org:10.1016/j.xcrp.2021.100515
70 Bourgot, I., Primac, I., Louis, T., Noel, A. & Maquoi, E. Reciprocal Interplay Between Fibrillar Collagens and Collagen-Binding Integrins: Implications in Cancer Progression and Metastasis. *Frontiers in oncology* **10** (2020). https://doi.org:ARTN 1488 10.3389/fonc.2020.01488
71 Correa-Gallegos, D., Jiang, D. S. & Rinkevich, Y. Fibroblasts as confederates of the immune system. *Immunol Rev* **302**, 147-162 (2021). https://doi.org:10.1111/imr.12972
72 Rognoni, E. *et al.* Role of distinct fibroblast lineages and immune cells in dermal repair following UV radiation-induced tissue damage. *eLife* **10** (2021). https://doi.org:10.7554/eLife.71052
73 Waldman, A. D., Fritz, J. M. & Lenardo, M. J. A guide to cancer immunotherapy: from T cell basic science to clinical practice. *Nat Rev Immunol* **20**, 651-668 (2020). https://doi.org:10.1038/s41577-020-0306-5
74 Rezzonico, R., Burger, D. & Dayer, J. M. Direct contact between T lymphocytes and human dermal fibroblasts or synoviocytes down-regulates types I and III collagen production via cell-associated cytokines. *J Biol Chem* **273**, 18720-18728 (1998). https://doi.org:DOI 10.1074/jbc.273.30.18720
75 Park, T. J. *et al.* Selective inflammatory pain insensitivity in the African naked mole-rat (Heterocephalus glaber). *PLoS Biol* **6**, e13 (2008). https://doi.org:10.1371/journal.pbio.0060013
76 Kemp, C. J. Multistep skin cancer in mice as a model to study the evolution of cancer cells. *Seminars in cancer biology* **15**, 460-473 (2005). https://doi.org:10.1016/j.semcancer.2005.06.003
77 Martins, V. C. *et al.* Cell competition is a tumour suppressor mechanism in the thymus. *Nature* **509**, 465-+ (2014). https://doi.org:10.1038/nature13317
78 Demeter, M., Derenyi, I. & Szollosi, G. J. Trade-off between reducing mutational accumulation and increasing commitment to differentiation determines tissue organization. *Nat Commun* **13**, 1666 (2022). https://doi.org:10.1038/s41467-022-29004-1
79 Ge, H. M., Tian, M. X., Pei, Q., Tan, F. B. & Pei, H. P. Extracellular Matrix Stiffness: New Areas Affecting Cell Metabolism. *Frontiers in oncology* **11** (2021). https://doi.org:ARTN 631991 10.3389/fonc.2021.631991
80 Najafi, M., Farhood, B. & Mortezaee, K. Extracellular matrix (ECM) stiffness and degradation as cancer drivers. *Journal of Cellular Biochemistry* **120**, 2782-2790 (2019). https://doi.org:10.1002/jcb.27681
81 Rognoni, E. & Watt, F. M. Skin Cell Heterogeneity in Development, Wound Healing, and Cancer. *Trends Cell Biol* **28**, 709-722 (2018). https://doi.org:10.1016/j.tcb.2018.05.002
82 Sahai, E. *et al.* A framework for advancing our understanding of cancer-associated fibroblasts. *Nature Reviews Cancer* **20**, 174-186 (2020). https://doi.org:10.1038/s41568-019-0238-1
83 Alkasalias, T., Moyano-Galceran, L., Arsenian-Henriksson, M. & Lehti, K. Fibroblasts in the Tumor Microenvironment: Shield or Spear? *International Journal of Molecular Sciences* **19** (2018). https://doi.org:ARTN 1532 10.3390/ijms19051532
84 Czekay, R. P., Cheon, D. J., Samarakoon, R., Kutz, S. M. & Higgins, P. J. Cancer-Associated Fibroblasts: Mechanisms of Tumor Progression and Novel Therapeutic Targets. *Cancers (Basel)* **14** (2022). https://doi.org:10.3390/cancers14051231
85 Pascual, G. *et al.* Targeting metastasis-initiating cells through the fatty acid receptor CD36. *Nature* **541**, 41-45 (2017). https://doi.org:10.1038/nature20791
86 Hafemeister, C. & Satija, R. Normalization and variance stabilization of single-cell RNA-seq data using regularized negative binomial regression. *Genome Biol* **20**, 296 (2019). https://doi.org:10.1186/s13059-019-1874-1
87 Satija, R., Farrell, J. A., Gennert, D., Schier, A. F. & Regev, A. Spatial reconstruction of single-cell gene expression data. *Nat Biotechnol* **33**, 495-502 (2015). https://doi.org:10.1038/nbt.3192
88 Lun, A. T., McCarthy, D. J. & Marioni, J. C. A step-by-step workflow for low-level analysis of single-cell RNA-seq data with Bioconductor. *F1000Res* **5**, 2122 (2016). https://doi.org:10.12688/f1000research.9501.2
89 Anders, S. & Huber, W. Differential expression analysis for sequence count data. *Genome Biol* **11**, R106 (2010). https://doi.org:gb-2010-11-10-r106 [pii] 10.1186/gb-2010-11-10-r106
90 Liberzon, A. *et al.* The Molecular Signatures Database (MSigDB) hallmark gene set collection. *Cell Syst* **1**, 417-425 (2015). https://doi.org:10.1016/j.cels.2015.12.004
91 Van der Auwera, G. A. *et al.* From FastQ data to high confidence variant calls: the Genome Analysis Toolkit best practices pipeline. *Curr Protoc Bioinformatics* **43**, 11 10 11-11 10 33 (2013). https://doi.org:10.1002/0471250953.bi1110s43
92 Aibar, S. *et al.* Identification of expression patterns in the progression of disease stages by integration of transcriptomic data. *BMC Bioinformatics* **17**, 432 (2016). https://doi.org:10.1186/s12859-016-1290-4
93 Haydont, V., Neiveyans, V., Fortunel, N. O. & Asselineau, D. Transcriptome profiling of human papillary and reticular fibroblasts from adult interfollicular dermis pinpoints the 'tissue skeleton' gene network as a component of skin chrono-ageing. *Mech Ageing Dev* **179**, 60-77 (2019). https://doi.org:10.1016/j.mad.2019.01.003
94 Janson, D. G., Saintigny, G., van Adrichem, A., Mahe, C. & El Ghalbzouri, A. Different gene expression patterns in human papillary and reticular fibroblasts. *J Invest Dermatol* **132**, 2565-2572 (2012). https://doi.org:10.1038/jid.2012.192

95 Nauroy, P. *et al.* Human Dermal Fibroblast Subpopulations Display Distinct Gene Signatures Related to Cell Behaviors and Matrisome. *J Invest Dermatol* **137**, 1787-1789 (2017). https://doi.org:10.1016/j.jid.2017.03.028
96 Philippeos, C. *et al.* Spatial and Single-Cell Transcriptional Profiling Identifies Functionally Distinct Human Dermal Fibroblast Subpopulations. *J Invest Dermatol* **138**, 811-825 (2018). https://doi.org:10.1016/j.jid.2018.01.016
97 Erez, N., Truitt, M., Olson, P., Arron, S. T. & Hanahan, D. Cancer-Associated Fibroblasts Are Activated in Incipient Neoplasia to Orchestrate Tumor-Promoting Inflammation in an NF-kappaB-Dependent Manner. *Cancer Cell* **17**, 135-147 (2010). https://doi.org:10.1016/j.ccr.2009.12.041
98 Galbo, P. M., Jr., Zang, X. & Zheng, D. Molecular Features of Cancer-associated Fibroblast Subtypes and their Implication on Cancer Pathogenesis, Prognosis, and Immunotherapy Resistance. *Clin Cancer Res* **27**, 2636-2647 (2021). https://doi.org:10.1158/1078-0432.CCR-20-4226
99 Butler, A., Hoffman, P., Smibert, P., Papalexi, E. & Satija, R. Integrating single-cell transcriptomic data across different conditions, technologies, and species. *Nat Biotechnol* **36**, 411-420 (2018). https://doi.org:10.1038/nbt.4096
100 Stuart, T. *et al.* Comprehensive Integration of Single-Cell Data. *Cell* **177**, 1888-1902 e1821 (2019). https://doi.org:10.1016/j.cell.2019.05.031
101 Vento-Tormo, R. *et al.* Single-cell reconstruction of the early maternal-fetal interface in humans. *Nature* **563**, 347-353 (2018). https://doi.org:10.1038/s41586-018-0698-6

Figure 1

1165

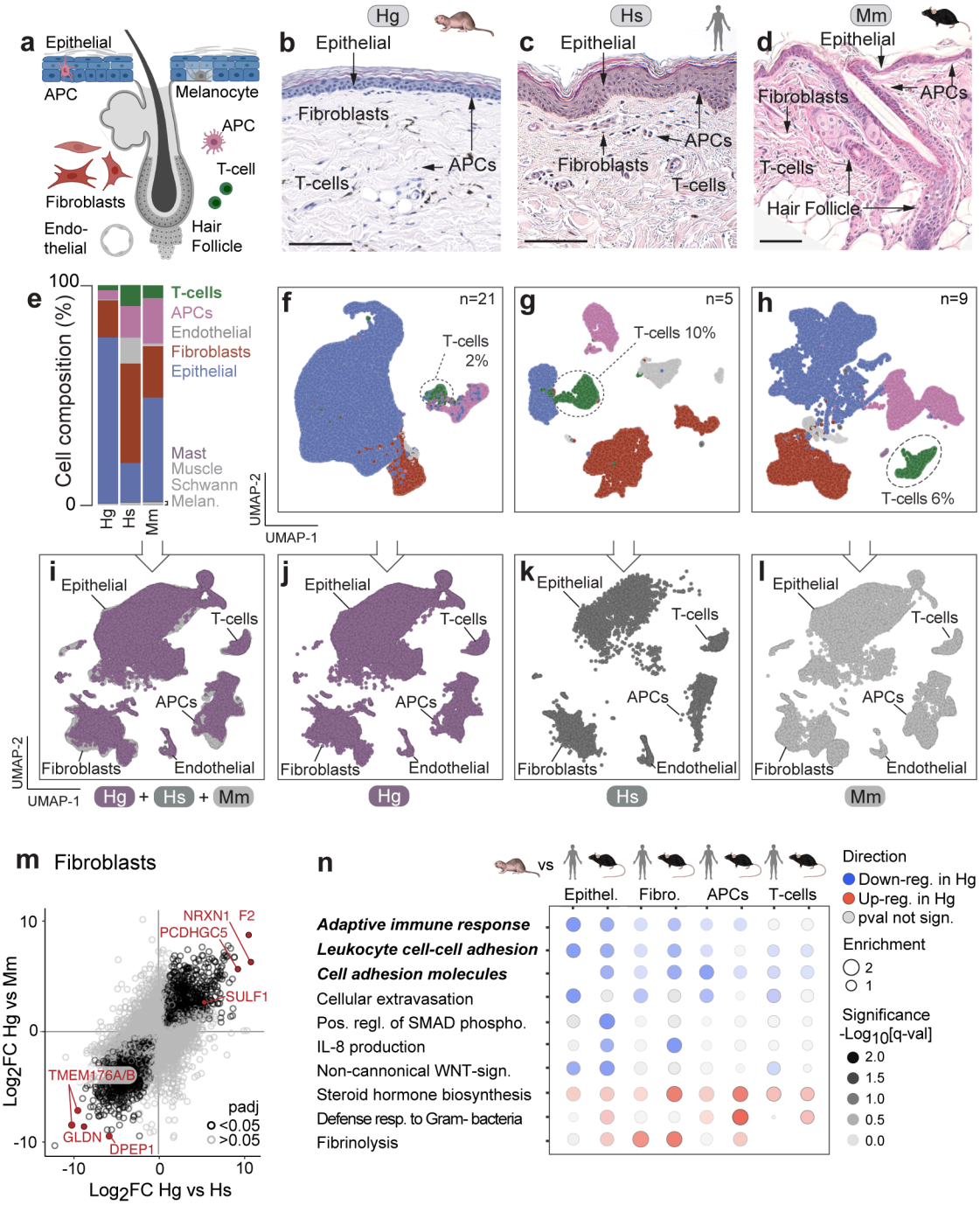

1170 **Figure 1. Species-specific features of cell-type composition in naked mole-rat skin**.
a-d, Illustration (a) and histology (haematoxylin and eosin) of naked mole-rat (Hg) (b), human (Hs) (c) and mouse (Mm) (d) skin. APCs: Antigen-presenting cells. Scale bars: 100 μm. **e-h**, Cell composition (e) and UMAPs (f-h) for each species colour coded by cell type, with number of biological replicates indicated. **i**, Integrated UMAP displaying all cells from all species, co-
1175 analysed using 1:1:1 orthologous genes. **j-l**, Per-species contributions to the integrated UMAP shown in (i) from Hg (j), Hs (k), and Mm (l), respectively. **m,** Correlation of fibroblast gene expression in Hg versus Hs (x-axis) and Hg versus Mm (y-axis). Black circles: significant genes (adjusted $P < 0.05$). **n,** Gene set enrichment analysis of differential functional pathways in Hg epithelial cells, fibroblasts, APCs and T-cells, versus Hs and Mm. Colour indicates
1180 enriched gene sets in up- (red) or down- (blue) regulated (reg.) genes in Hg, size of circle is enrichment, and statistical significance is shown by shading**.**

Figure 2

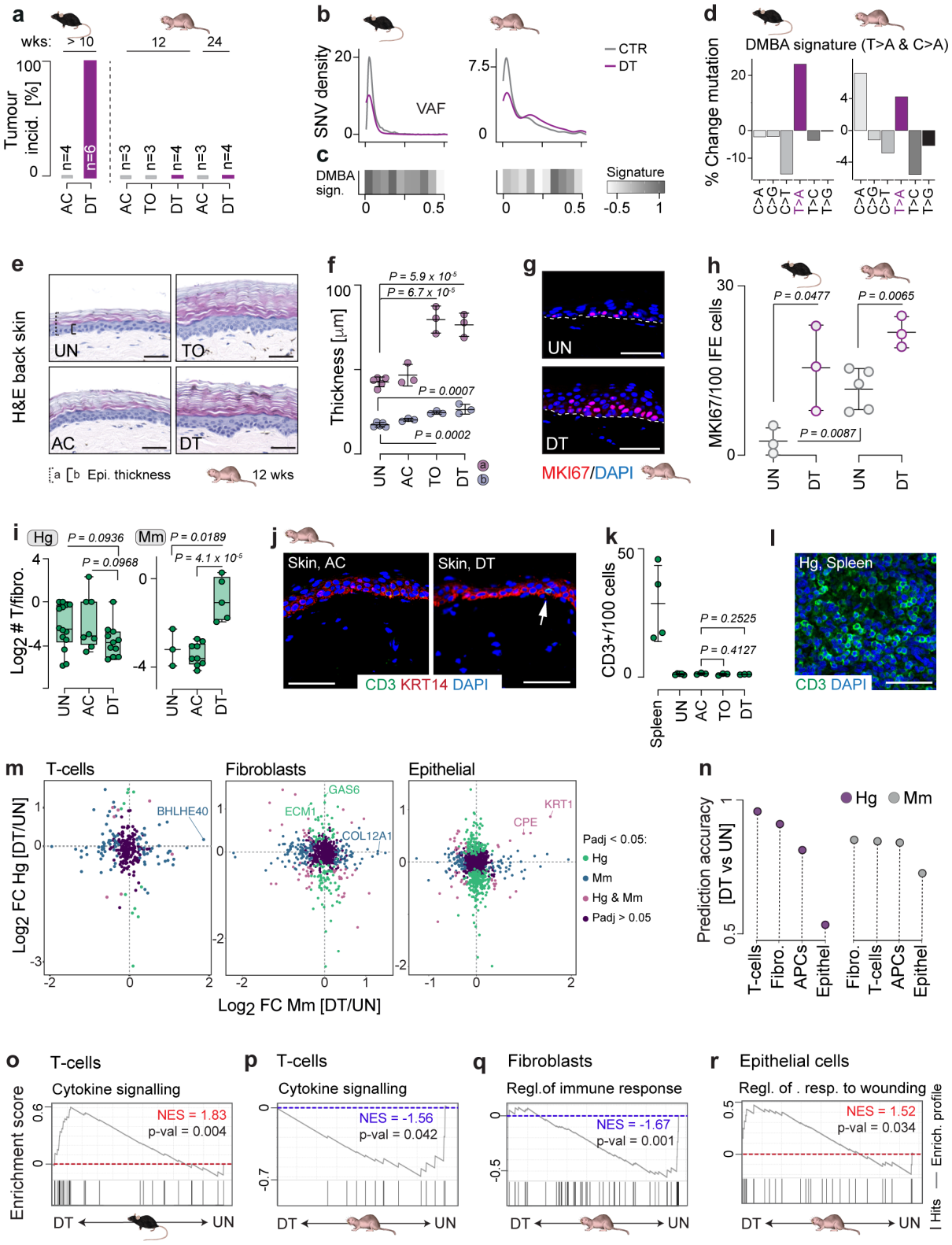
a
wks: > 10
12
24
Tumour incid. [%]
n=4
n=6
n=3
n=3
n=4
n=3
n=4
AC
DT
AC
TO
DT
AC
DT
b
SNV density
VAF
CTR
DT
c
DMBA sign.
Signature
d
DMBA signature (T>A & C>A)
% Change mutation
C>A
C>G
C>T
T>A
T>C
T>G
e
H&E back skin
UN
TO
AC
DT
Epi. thickness
12 wks
f
Thickness [µm]
P = 5.9 x 10-5
P = 6.7 x 10-5
P = 0.0007
P = 0.0002
UN
AC
TO
DT
g
UN
DT
MKI67/DAPI
h
MKI67/100 IFE cells
P = 0.0477
P = 0.0065
P = 0.0087
UN
DT
UN
DT
i
Hg
P = 0.0936
P = 0.0968
Mm
P = 0.0189
P = 4.1 x 10-5
Log2 # T/fibro.
UN
AC
DT
UN
AC
DT
j
Skin, AC
Skin, DT
CD3 KRT14 DAPI
k
CD3+/100 cells
P = 0.2525
P = 0.4127
Spleen
UN
AC
TO
DT
l
Hg, Spleen
CD3 DAPI
m
T-cells
Fibroblasts
Epithelial
BHLHE40
GAS6
ECM1
COL12A1
KRT1
CPE
Padj < 0.05:
Hg
Mm
Hg & Mm
Padj > 0.05
Log2 FC Hg [DT/UN]
Log2 FC Mm [DT/UN]
n
Hg
Mm
Prediction accuracy [DT vs UN]
T-cells
Fibro.
APCs
Epithel
Fibro.
T-cells
APCs
Epithel
o
T-cells
Cytokine signalling
NES = 1.83
p-val = 0.004
Enrichment score
DT
UN
p
T-cells
Cytokine signalling
NES = -1.56
p-val = 0.042
DT
UN
q
Fibroblasts
Regl.of immune response
NES = -1.67
p-val = 0.001
DT
UN
r
Epithelial cells
Regl. of . resp. to wounding
NES = 1.52
p-val = 0.034
Enrich. profile
Hits
DT
UN

1190 **Figure 2. Naked mole-rats are resistant to chemically induced epithelial tumours**

a, Percentage of skin tumour incidences (incid.) in animals treated with acetone (AC), DMBA/TPA (DT), or TPA only (TO) for 10 weeks (wks) in mouse (black icon), or for 12 and 24 wks in naked mole-rats (beige icon). **b-c,** Single nucleotide variant allelic frequency (VAF) density plots (b) and heatmap of DMBA mutational signature occurrence (c) in control (CTR) 1195 or DT-treated mice (left panels) and naked mole-rat (right panels). **d**, Change in types of single-nucleotide substitutions upon DT treatment. **e,** Histology (haematoxylin and eosin) of naked mole-rat back skin sections untreated (UN) or treated as indicated a for 12 wks. Solid bracket: thickness of epidermis; dotted bracket: epidermal thickness including cornified envelope. **f,** Quantification of naked mole-rat epidermal thickness including (purple) or excluding (blue) 1200 cornified envelope after the indicated treatments. **g,** Immunofluorescence of MKI67-positive interfollicular epidermal (IFE) cells in UN or DT-treated naked mole-rat skin. White dotted line: basement membrane. **h.** Quantification of (g) shows relative increase of MKI67 positive following DT treatment by species. **i**, Log_2 fold change of T-cells versus fibroblasts by condition, calculated using scRNA-seq in naked mole-rat (Hg) and mouse (Mm) skin. Box 1205 plots show first quartile, median, and third quartile. **j-l**, Immunofluorescence (j,l) and quantification (k) of CD3-expressing Hg T-cells in skin (j) and spleen (l) after the indicated treatments. Keratin 14 (KRT14) stained basal epithelial cells. Arrow: CD3-positive cell. Spleen is a positive control tissue for CD3-antibody specificity. DAPI: nuclear counterstain (g,j,l). Scale bars: 50 μm (e,g,j,l). **m**, Correlation of Hg (y-axis) versus Mm (x-axis) orthologous genes 1210 differentially expressed in each cell-type upon DT treatment (adjusted $P < 0.05$), coloured by species-specificity with Hg (green), Mm (blue), both (pink), or non-significant (adjusted $P > 0.05$) (dark purple). **n**, Prediction accuracy of transcriptional responses to DT treatment in Hg (purple) and Mm (grey) cell types. **o-r,** Gene set enrichment analysis of differentially expressed genes upon DT treatment in Mm (o) or Hg (p) T-cells or Hg fibroblasts (q) and epithelial cells 1215 (r). NES: Normalised enrichment score. Shown is mean ± s.d. (f,h,i,k). Unpaired two-tailed unpaired *t*-test (f,h,i,k). Exact *P*-values are indicated.

Figure 3

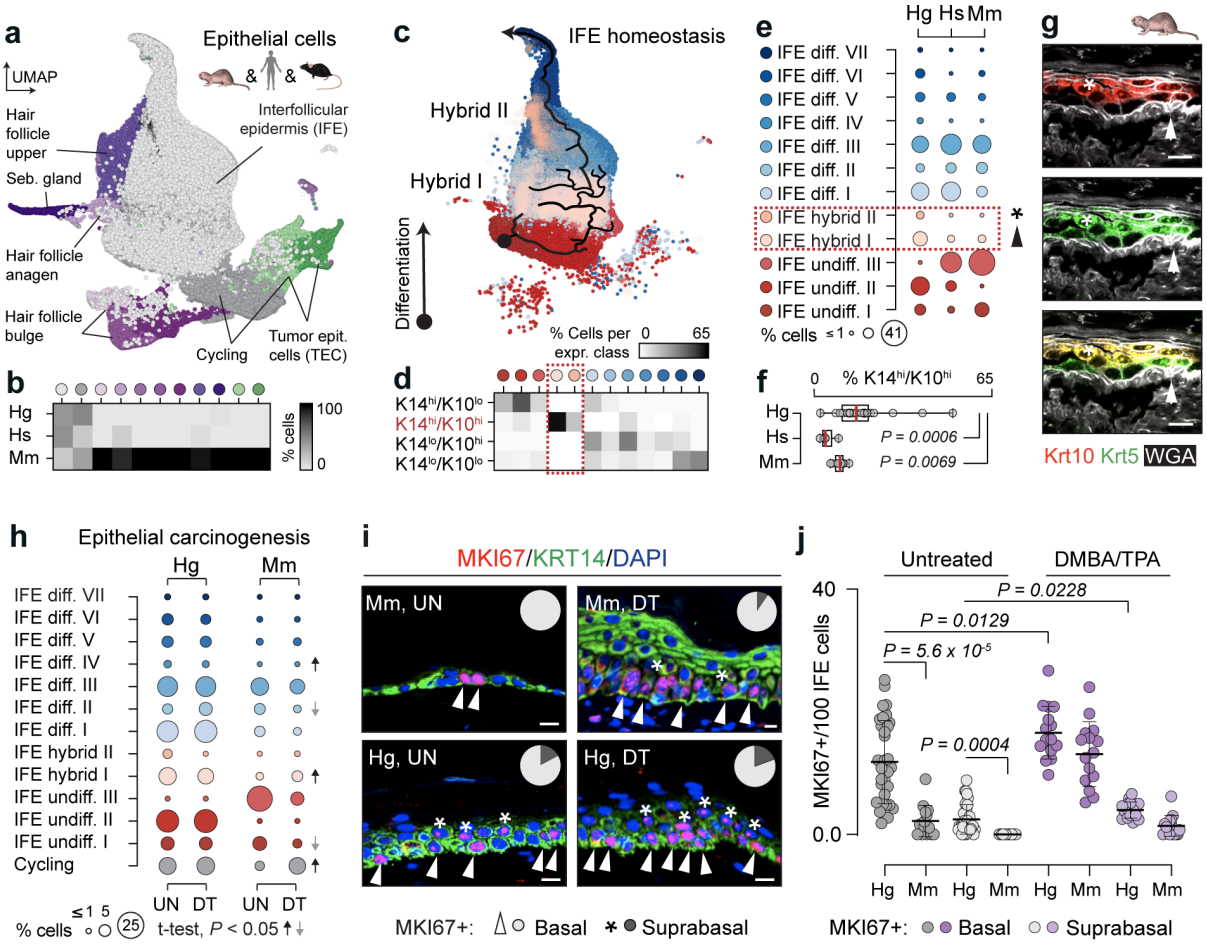
a
Epithelial cells
UMAP
Hair follicle upper
Seb. gland
Interfollicular epidermis (IFE)
Hair follicle anagen
Hair follicle bulge
Cycling
Tumor epit. cells (TEC)
b
Hg
Hs
Mm
% cells
100
0
c
IFE homeostasis
Hybrid II
Hybrid I
Differentiation
% Cells per expr. class
0
65
d
K14hi/K10lo
K14hi/K10hi
K14lo/K10hi
K14lo/K10lo
e
Hg Hs Mm
IFE diff. VII
IFE diff. VI
IFE diff. V
IFE diff. IV
IFE diff. III
IFE diff. II
IFE diff. I
IFE hybrid II
IFE hybrid I
IFE undiff. III
IFE undiff. II
IFE undiff. I
% cells ≤1 41
f
% K14hi/K10hi
P = 0.0006
P = 0.0069
g
Krt10 Krt5 WGA
h
Epithelial carcinogenesis
Hg
Mm
Cycling
UN DT UN DT
% cells ≤1 5 25
t-test, P < 0.05
i
MKI67/KRT14/DAPI
Mm, UN
Mm, DT
Hg, UN
Hg, DT
MKI67+: Basal Suprabasal
j
Untreated
DMBA/TPA
MKI67+/100 IFE cells
40
0.0
P = 0.0228
P = 0.0129
P = 5.6 x 10-5
P = 0.0004
Hg Mm Hg Mm Hg Mm Hg Mm
MKI67+: Basal Suprabasal
k
KRT10/KRT14/DAPI
UN
DT
l
KRT10+/100 basal cells
40
0
P = 0.0007
P = 0.0062
UN DT UN DT
m
Clone 1
Clone 2
n
Progenitor replacement rate
0.25
0.05
P = 3.2 x 10-5
Hg Mm

Figure 3. Accelerated epidermal turn-over in naked mole-rat maintains skin integrity.

a, UMAP of epithelial cells in all three species. Seb.: Sebaceous gland. **b,** Weighted average percent of each epithelial cell type per species. **c,** UMAP of all species' interfollicular epidermal (IFE) cells, with overlaid calculated pseudotime differentiation trajectory, starting from lower left black dot. Colours indicate cell differentiation states. **d**, Percentage of IFE cells in keratin (K) 14 or K10 high (hi) or low (lo) expression class. Dotted red box: IFE hybrid I and II differentiation cell states. **e**, Dot plot showing percentage of cells per IFE differentiation state in naked mole-rat (Hg), human (Hs) and mouse (Mm). **f**, Percentage of $K14^{hi}/K10^{hi}$ cells in skin biopsies by species. **g**, RNAscope labelling for keratin (Krt) 10 and Krt5 in Hg skin sections. WGA: plasma membrane label. Arrowhead: IFE hybrid. Asterisk: IFE hybrid II cells. **h**, Proportion of cell state frequencies in untreated (UN) versus DMBA/TPA treated (DT) Hg and Mm skin. Only Mm cell state frequencies change significantly ($P < 0.05$) in the direction of the arrows. **i-j**, Immunofluorescence (i) and quantification (j) of MKI67-positive epidermal cells in UN and DT Hg and Mm skin sections. Pie charts: fraction of basal (white) and suprabasal (grey) MKI67-positive cells. Arrowheads: MKI67-positive basal cells. Asterisks: MKI67-positive suprabasal cells. KRT14 marks undifferentiated cells. **k-l**, Immunofluorescence (k) and quantification (l) of KRT14/KRT10 double-positive basal cells in UN and DT treated Hg skin. Boxed insets: magnified area (lower panels). Arrows: KRT14/KRT10-positive cells. **m**, Illustration of how clonal expansion can alter somatic mutation frequencies. **n**, Clonal expansion is used to measure progenitor replacement rates in Hg and Mm after exposure to DT. DAPI: nuclear counterstain (i,k). Scale bars 10 μm (g,i,k). Box plots show minimum value, first quartile, median (red line), third quartile and maximum value (f, n). Shown is mean ± s.d. (N = 3 individuals) (j,l). Unpaired two-tailed *t*-test (f, h, j, l, n). Exact *P* values are indicated.

Figure 4

1255

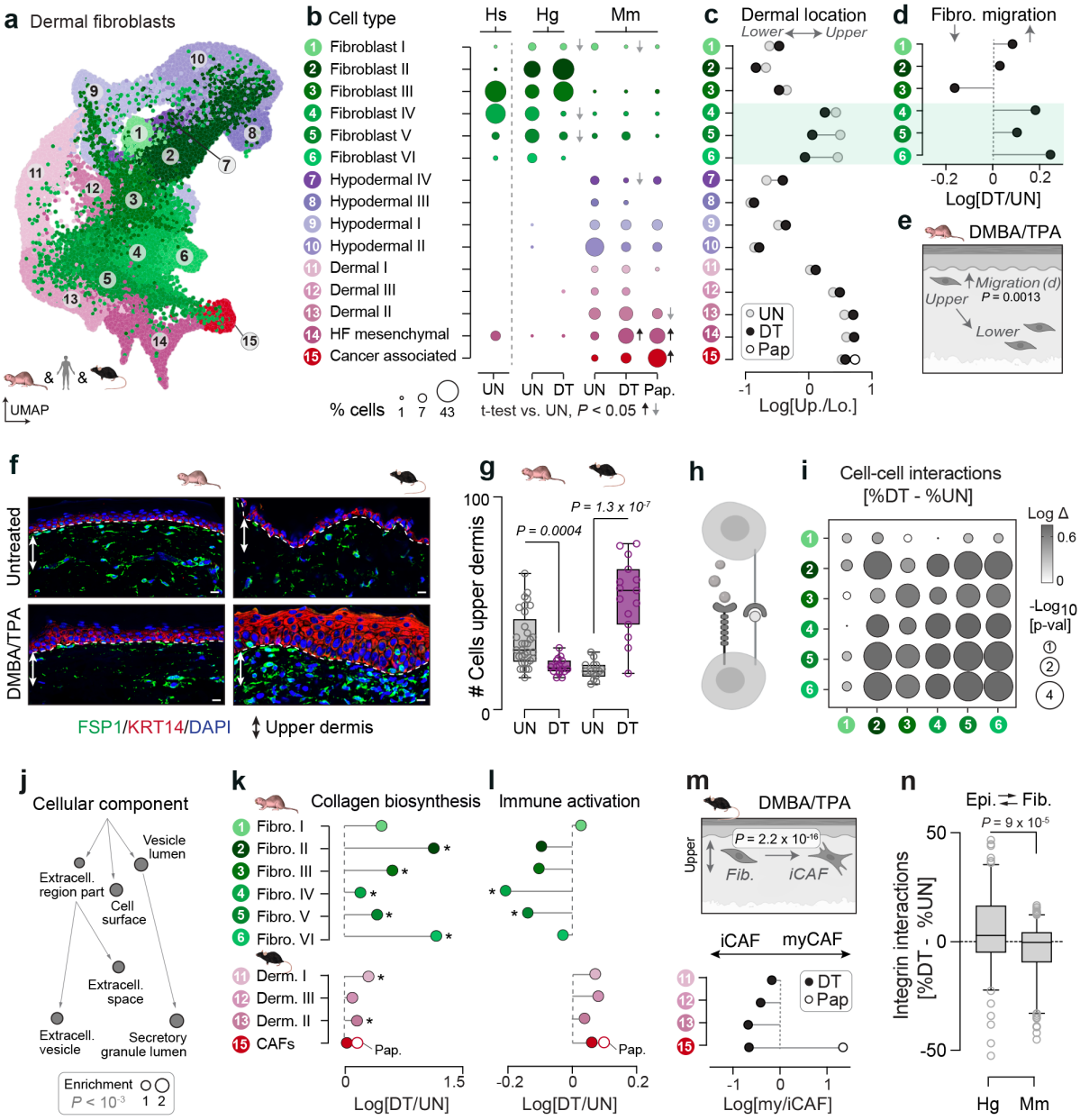

1260 **Figure 4. Naked mole-rat does not create pro-tumorigenic niches.**

a-b, UMAP (a) and cell state assignment (b) of skin fibroblasts from naked mole-rat (Hg), human (Hs) and mouse (Mm), sorted by condition: untreated (UN), DMBA/TPA (DT) treated, and papilloma (Pap.). HF: Hair follicle. Arrows: significantly ($P < 0.05$) increased (black) and decreased (grey) cell proportions. **c,** Predicted location of fibroblasts in the upper or lower
1265 dermis before and after DT treatment in Hg (class 1-6) and Mm (class 7-15). **d-e**, Transcriptional signatures in fibroblasts in class 1-6 (d) identify significantly ($P = 0.0013$) (e) enhanced migration in the upper dermis following DT treatment. **f-g**, Immunofluorescence of Fibroblast-specific protein 1 (FSP1) and keratin 14 (KRT14) (f) and number of cells in the upper dermis (g) in UN and DT treated skin of Mm and Hg. Dotted line: Basement membrane.
1270 Double arrow: Upper dermis (40 μm). DAPI: nuclear counterstain. Scale bar: 10 μm. **h-i**, Illustration of cell-cell interactions (h) and changes in cell-cell communications (i) between fibroblasts of class 1-6 following DT treatment shown as log ratio (log Δ) of percentage of significant interactions in DT over percentage of significant interactions in UN. **j**, Gene ontology analysis (GOrilla; cellular component) using significantly differently (adjusted $P <$
1275 0.05) expressed genes in all Hg fibroblasts combined. Background: All expressed genes. Extracell.: Extracellular. **k-l**, Natural log transformed (Log) ratio of gene sets scores for collagen biosynthesis (k) and immune activation (l) comparing DT (filled circle) or Pap. (non-filled circle) over UN for indicated fibroblast subtype. **m**, Illustration (top) and Log ratio (bottom) of myofibroblasts over pro-inflammatory cancer associated fibroblasts
1280 (myCAF/iCAF) gene sets scores in DT (black circle) and Pap. (white circle) fibroblast subtype 11-13 and 15. **n**, Percent change in UN and DT cell-cell integrin interactions across all epithelial cells (Epi.) and fibroblasts (Fib.) in Hg and Mm skin. Box plots show first quartile, median, and third quartile (g) or median and whiskers at 5 and 95 percentiles (n). *: $P < 0.05$ (k-l). Unpaired two-tailed unpaired *t*-test (g). F-test (n). *P* value for interaction term between
1285 dermal location and treatment in a linear mixed-effects model describing fibroblast migration score (e) and myCAF/iCAF ratio (m).

Figure 5

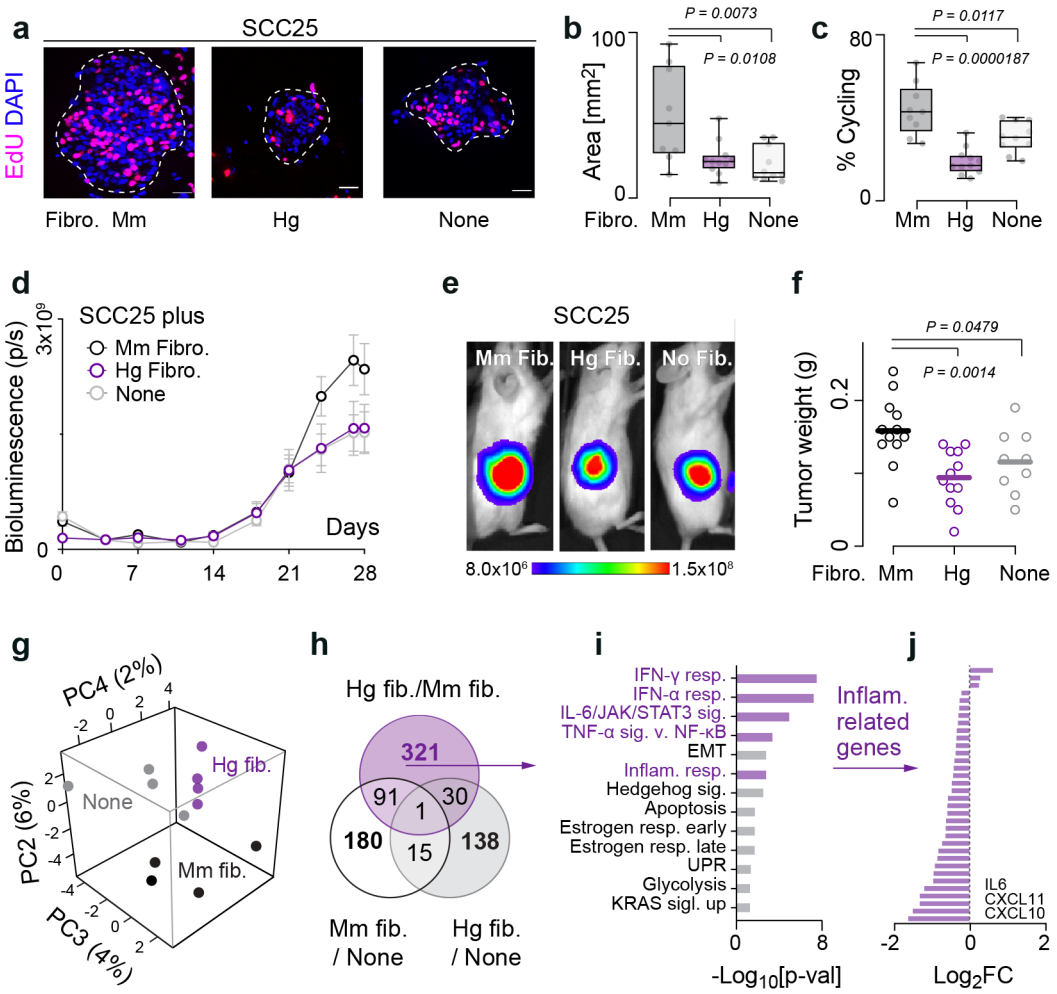
a
SCC25
EdU DAPI
Fibro. Mm
Hg
None
b
P = 0.0073
P = 0.0108
Area [mm2]
100
0
Fibro. Mm Hg None
c
P = 0.0117
P = 0.0000187
% Cycling
80
0
Mm Hg None
d
SCC25 plus
Mm Fibro.
Hg Fibro.
None
Bioluminescence (p/s)
3x10^9
0
Days
0 7 14 21 28
e
SCC25
Mm Fib.
Hg Fib.
No Fib.
8.0x10^6
1.5x10^8
f
P = 0.0479
P = 0.0014
Tumor weight (g)
0.2
0
Fibro. Mm Hg None
g
PC4 (2%)
PC2 (6%)
PC3 (4%)
Hg fib.
None
Mm fib.
h
Hg fib./Mm fib.
321
91
30
1
180
15
138
Mm fib. / None
Hg fib. / None
i
IFN-γ resp.
IFN-α resp.
IL-6/JAK/STAT3 sig.
TNF-α sig. v. NF-κB
EMT
Inflam. resp.
Hedgehog sig.
Apoptosis
Estrogen resp. early
Estrogen resp. late
UPR
Glycolysis
KRAS sigl. up
0 8
-Log10[p-val]
j
Inflam. related genes
IL6
CXCL11
CXCL10
-2 0 2
Log2FC

1295 **Figure 5. Naked mole-rat fibroblasts suppress tumour growth.**

a-c, Immunofluorescence for EdU (a) and quantification of area (b) and percentage of cycling cells (c) of tumouroids formed through co-culture of human squamous cell carcinoma (SCC25) cells with mouse (Mm), naked mole-rat (Hg), or no fibroblasts (None). DAPI: nuclear counterstain (a). N = 9-11 tumouroids. Scale bar: 10 μm. (a-c). **d-f.** Quantification of
1300 xenografts' growth (d), bioluminescence images of tumours in mice (e) and tumour weight (f) after 28 days of co-injected SCC25 cells with Mm, Hg, or no fibroblasts. N = 5 mice per condition. **g**, RNA sequencing followed by dimensionality reduction. N = 4 xenografts per condition. **h**, Overlap of significantly ($P < 0.01$) differentially expressed genes among the indicated datasets. **i**, Inflammatory and signalling responses (purple) were enriched among the
1305 321 genes differently expressed between tumours co-injected with Hg versus Mm fibroblasts (EnrichR). EMT: Epithelial-to-Mesenchymal Transition; UPR: Unfolded protein response. **j**, Inflammation (Inflam.) related genes from (i) are repressed in tumours co-injected with Hg fibroblasts when compared Mm fibroblasts co-injected tumours. Box plots show minimum value, first quartile, median, third quartile and maximum value (b,c). Shown is mean (f).
1310 Unpaired two-tailed *t*-test (b, c, f). Exact *P* values are indicated.

Extended Data Figure 1

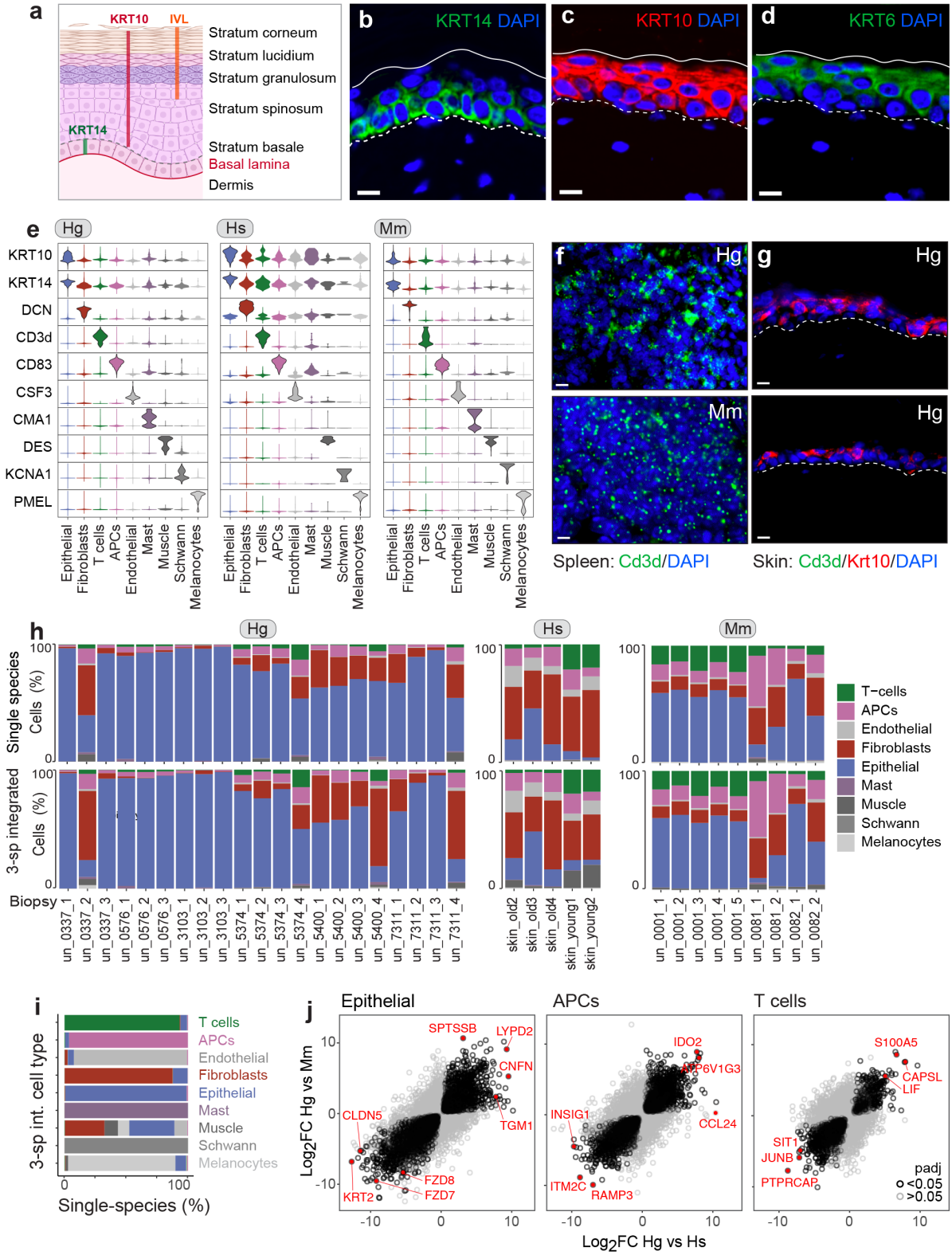

1315

Extended Data Figure 1. Comparative analyses of skin cell types in naked mole-rat, mouse and human. a-d, Illustration of epidermal cell layers (a) and immunofluorescence (b-d) for keratin 14 (KRT14) (b), KRT10 (c), and KRT6 (d) in naked mole-rat back skin sections. **e**, Marker genes identifying the indicated cell types in naked mole-rat (Hg), human (Hs) and mouse (Mm). **f-g**, RNAscope to detect *Cd3d* in spleen (f) and skin (g) section from Mm and Hg. KRT10: suprabasal stain. DAPI: nuclear counterstain. Dotted lines: basement membrane (b-d,f,g). Solid lines: outer cornified envelope. Scale bars: 10 μm (b-d,f,g). **h**, Proportion of the cell types in the individual (top) or after 3-species (3-sp) integration (bottom) in Hg, Hs and Mm biopsies. **i**, Cell types classified after 3-species integration and mapped to their single species cell annotation. **j**, Correlation of epithelial (left), antigen presenting (APC) (middle) and T- (right) cells gene expression in Hg versus Hs (x-axis) and Hg versus Mm (y-axis). Black circles: significant genes (adjusted $P < 0.05$).

Extended Data Figure 2

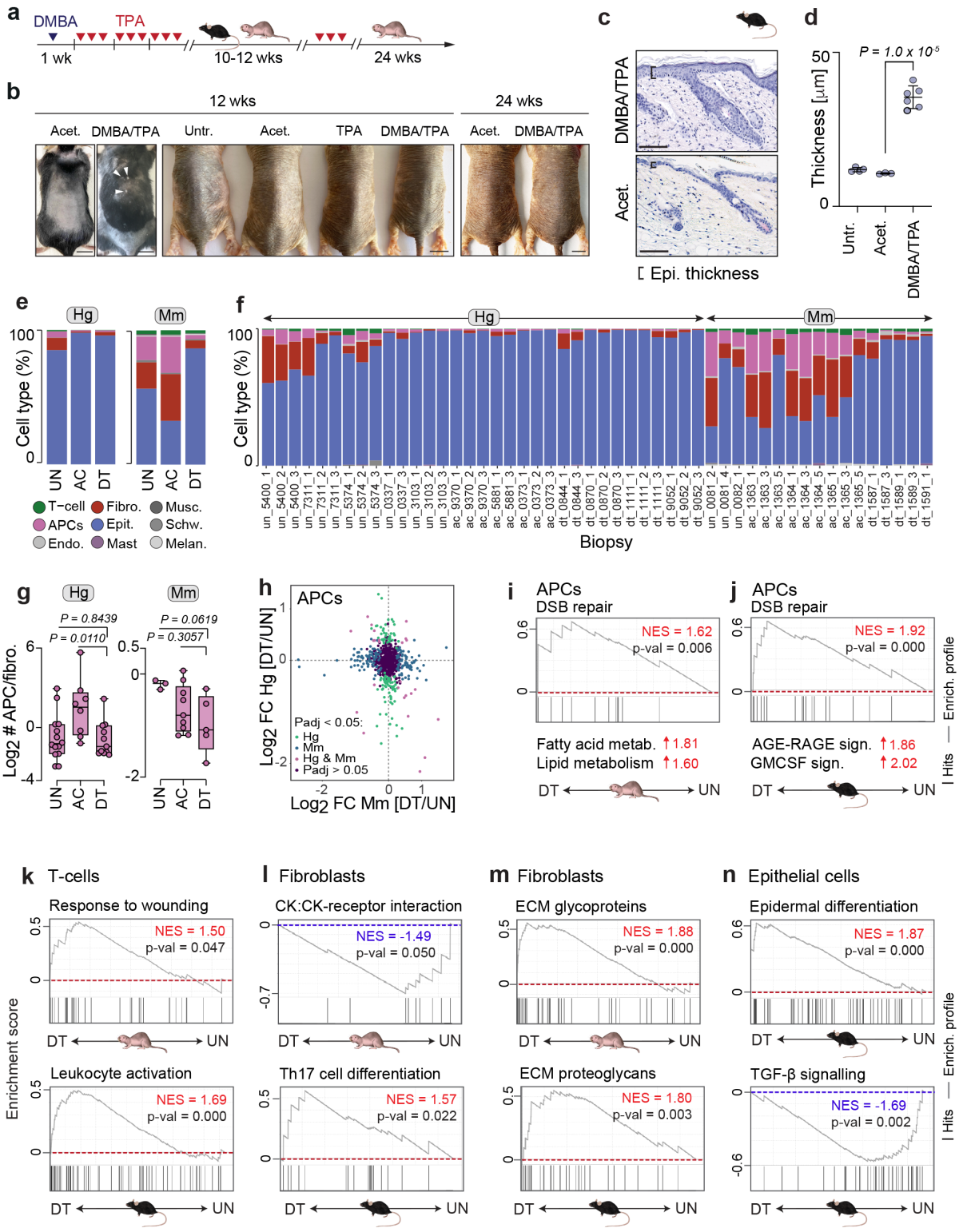

1335

Extended Data Figure 2. Chemical-induced carcinogenesis affects naked mole-rat and mouse skin differently. a, Carcinogenesis protocol using DMBA/TPA (DT). Wk/s: week/s. **b,** Representative images of mice and naked mole-rats treated with DT or the respective controls. Untr.: untreated. Acet.: acetone. TPA: only TPA for 12 or 24 wks. Arrow head: papillomas. **c-d,** Mouse skin histology (hematoxylin and eosin) (c) and epidermal (Epi.) thickness quantification (d) following the indicated treatments. Bracket: epidermis 10-12 weeks after cancer induction. Scale bars: 1cm (b), 50 μm (c). **e-f**, Proportion of the indicated cell types in all (e) and individual (f) biopsies of untreated (UN) or acetone (AC) and DT-treated naked mole-rat (Hg) and mouse (Mm) skin. APCs: Antigen-presenting cells, Endo.: Endothelial, Fibro.: Fibroblasts, Epit.: Epithelial, Musc: Muscle, Schw.: Schwann, Melan: Melanocytes. **g,** Log2 fold change of APCs over fibroblasts (fibro.) in UN, AC and DT Hg (left) and Mm (right) skin. **h,** Correlation of significantly (adjusted $p<0.05$) differentially expressed genes in APCs from Hg (green), Mm (blue), both (pink), and non-significant (adjusted $P > 0.05$) (dark purple). **i-n,** Gene set enrichment analysis of differentially expressed genes in APCs (i,j), T-cells (k), fibroblasts (l,m), and epithelial cells (n) in naked mole-rat and mouse. Sign.: Signalling; DSB: Double strand break; CK: cytokine; TH17: T helper 17 cells; ECM: Extracellular matrix; TGF-β: Transforming growth factor β. NES: Normalised enrichment score. Shown is mean ± s.d. (d). Box plots show minimum value, first quartile, median, third quartile and maximum (g). Unpaired two-tailed t-test (g). Exact *P* values are indicated.

Extended Data Figure 3

1360

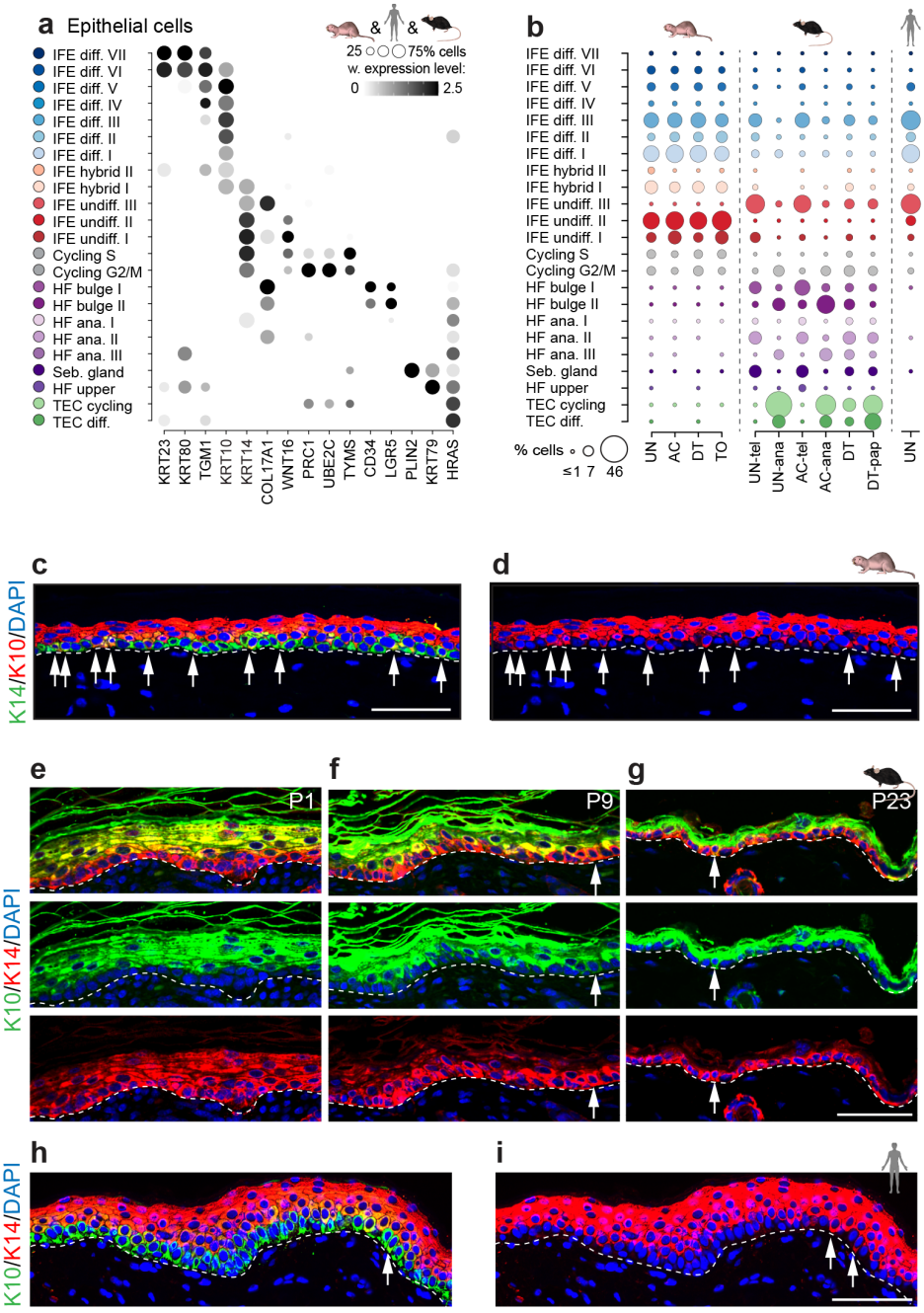

Extended Data Figure 3. High epidermal turn-over in naked mole-rat skin. a, Dot plot showing expression levels (shades) of orthologues genes used for classification of epithelial cells in naked mole-rat, human and mouse. Dot size: percentage of cells expressing the indicated gene. IFE: Interfollicular epidermis; diff: differentiated; undiff: undifferentiated; HF: hair-follicle; ana: anagen; Seb.: sebaceous, TEC: Tumour epithelial cell. **b**, Dot plot showing percentage of cells per IFE differentiation state by species in untreated (UN) and acetone (AC), DMBA/TPA (DT), or TPA (TO) treated skin. tel: telogen; ana: anagen; pap: papilloma. **c-i**, Immunofluorescence for keratin 14 (K14) and K10 in naked mole-rat (c,d), mouse (e-g) and human (h,j) skin sections. Arrows: basal K14/K10 double positive cells. Dotted lines: basement membrane. P1,9,23: Postnatal days 1, 9 and 23. DAPI: nuclear counter stain (c-i). Scale bars: 100 μm (c-i).

1375

Extended Data Figure 4

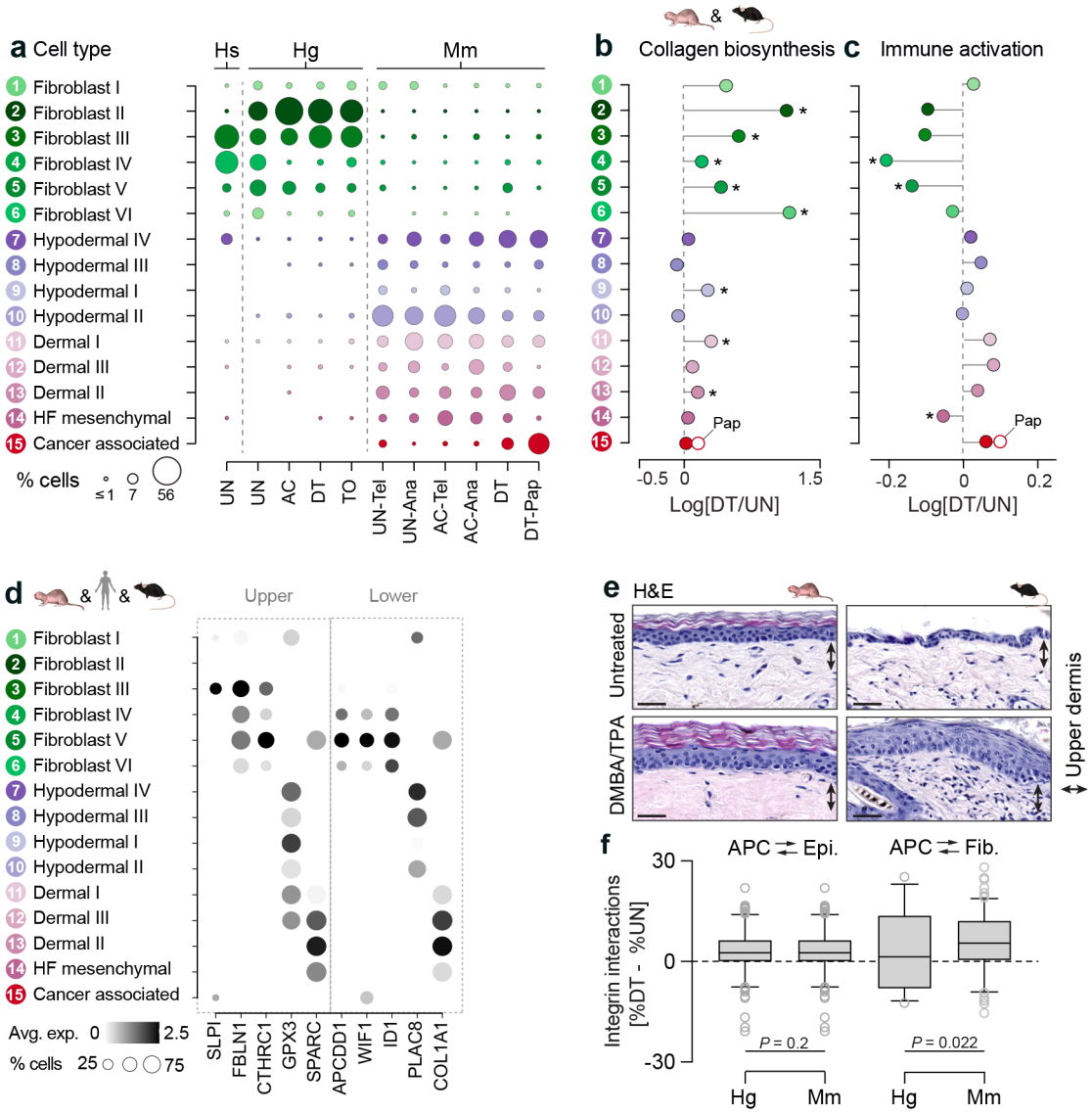

Extended Data Figure 4. Distinct responses to DMBA/TPA in naked mole-rat and mouse dermal fibroblasts. a, Cell state assignment of skin fibroblasts from naked mole-rat (Hg), human (Hs) and mouse (Mm), sorted by condition: untreated (UN) and acetone (AC), DMBA/TPA (DT), or TPA only (TO) treated, and papilloma (Pap). HF: Hair follicle. **b-c**, Natural log transformed ratio of gene sets scores for collagen biosynthesis (b) and immune activation (c) in DT over UN samples. **d**, Dot plot of average gene expression (shades) in all three species fibroblast sub-types. Dot sizes: percentage of cells expressing indicated gene. **e**, Histology (haematoxylin and eosin) of Hg and Mm skin sections. Double arrow: Upper dermis (40 μm). **f**, Integrin signalling between APC and epidermal (Epi) or stromal (Str) cells counted in Mm and Hg. Box plots show median and whiskers at 5 and 95 percentiles (f). *: $P < 0.05$. F-test (f).

Extended Data Figure 5

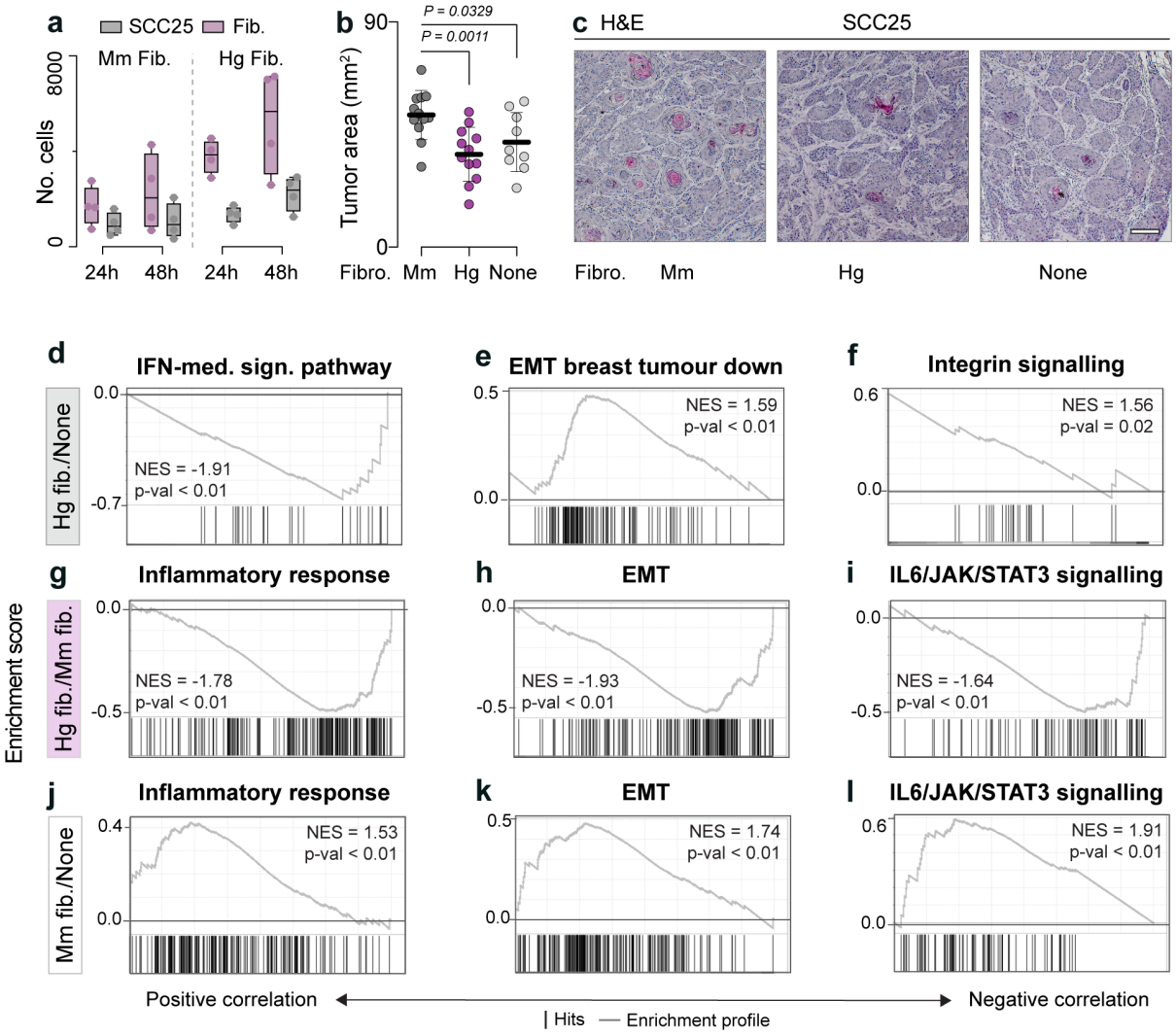

Extended Data Figure 5. Skin cancer-suppressive naked mole-rat interactions.

a, Number (No.) of fibroblasts (purple) and squamous cancer cells (SCC25) (grey) in tumouroids from co-cultures with mouse (Mm) or naked mole-rat (Hg) fibroblasts after 24 and 48 hours (h). **b-c,** Tumour area (b) and histology (haematoxylin and eosin) (c) of SCC25 xenografts co-injected with Mm, Hg or no fibroblasts (None). Scale bars: 100 μm. **d-l,** Significantly enriched pathways (GSEA) in RNA sequencing data from SCC25 tumours co-injected with Hg versus no fibroblasts (none) (d-f), Hg versus Mm fibroblasts (g-i) or Mm fibroblasts versus none (j-l). NES: Normalised enrichment score. IFN-med. sign. pathway: Interferon-mediated signalling pathway; EMT: Epithelial-to-Mesenchymal Transition. Box plots show minimum value, first quartile, median, third quartile and maximum value (a). Shown is mean ± s.d. (b). Unpaired two-tailed *t*-test (b). Exact *P* values are indicated (b).